

Learning collective variables that preserve transition rates

Shashank Sule ^{*1}, Arnav Mehta ^{†2}, and Maria K. Cameron ^{‡1}

¹Department of Mathematics, University of Maryland, College Park, MD, USA

²Department of Mathematics, University of California, Berkeley, CA, USA

June 11, 2025

Abstract

Collective variables (CVs) play a crucial role in capturing rare events in high-dimensional systems, motivating the continual search for principled approaches to their design. In this work, we revisit the framework of quantitative coarse graining and identify the orthogonality condition from Legoll and Lelievre (2010) as a key criterion for constructing CVs that accurately preserve the statistical properties of the original process. We establish that satisfaction of the orthogonality condition enables error estimates for both relative entropy and pathwise distance to scale proportionally with the degree of scale separation. Building on this foundation, we introduce a general numerical method for designing neural network-based CVs that integrates tools from manifold learning with group-invariant featurization. To demonstrate the efficacy of our approach, we construct CVs for butane and achieve a CV that reproduces the anti-gauche transition rate with less than ten percent relative error. Additionally, we provide empirical evidence challenging the necessity of uniform positive definiteness in diffusion tensors for transition rate reproduction and highlight the critical role of light atoms in CV design for molecular dynamics.

1 Introduction

Collective variable (CV) discovery is a fundamental problem in computational statistical physics involving the design of coarse-grained low-dimensional representations of high-dimensional stochastic processes. In practice, CV discovery is particularly important for the design of novel materials [Neh+22; Zha+19; Kar+21] or drug discovery [CPM15; ABG06] and for the understanding of rare events in molecular dynamics (MD) simulations of biomolecules

^{*}ssule25@umd.edu

[†]arnavmehta@berkeley.edu

[‡]mariakc@umd.edu

and chemical reactions [Yan+19; PNV19; VTP16]. A standard model for such MD simulations is the *overdamped Langevin dynamics*, which describes the motion of N coordinates in a potential energy landscape:

$$dX_t = -\nabla V(X_t) dt + \sqrt{2\beta^{-1}} dW_t. \quad (1)$$

Here $X_t \in \mathbb{R}^N$ represents the system's state, $V : \mathbb{R}^N \rightarrow \mathbb{R}$ is the potential energy function, $\beta^{-1} = k_B T$ where T is the temperature and k_B the Boltzmann constant, and W_t is a standard Wiener process. The wells of the potential V encode metastable states—regions where the system remains trapped for long periods before transitioning due to thermal fluctuations. Simulating and analyzing these transitions is computationally expensive due to the wide range of timescales involved. Therefore, instead of working directly with the high-dimensional process X_t , we seek a collective variable $\xi : \mathbb{R}^N \rightarrow \mathbb{R}^d$ that maps X_t to a low-dimensional process $Y_t = \xi(X_t)$. Typically, CVs are designed with the following objectives:

1. Mapping by ξ should separate metastable states, enabling a clear description of transitions,
2. The CV should enable enhanced sampling to accelerate rare-event simulations, and
3. The mapped process $Y_t = \xi(X_t)$ should reproduce the statistical properties of the original dynamics.

Thus, while traditional feature learning techniques in artificial intelligence optimize for expressivity or discriminative power, CVs must respect the dynamical and geometric properties of X_t , making their construction significantly more challenging. There is nonetheless a rich line of work for designing metastable state-separating CVs and CVs for enhanced sampling using data-driven methods, thus satisfying objectives (1) and (2). However, a key hindrance to achieving the objective (3) is that the projected process Y_t is generally not closed because its evolution depends not only on its current state but also on latent high-dimensional variables. This lack of closure makes direct simulation and statistical reproduction of Y_t infeasible. This is seen by applying Ito's lemma to $\xi(X_t)$:

$$dY_t = d\xi(X_t) = \mathcal{L}\xi(X_t) dt + \sqrt{2\beta^{-1}} \det(D\xi(X_t) D\xi(X_t)^\top)^{1/2} dB_t. \quad (2)$$

Here B_t is a rescaled Brownian motion in \mathbb{R}^d and \mathcal{L} is the infinitesimal generator of the overdamped Langevin dynamics (1):

$$B_t = \frac{D\xi}{\det(D\xi D\xi^\top)^{1/2}} W_t, \quad (3)$$

$$\mathcal{L}f := \beta^{-1} \Delta f - \nabla V \cdot \nabla f. \quad (4)$$

One approach to constructing a closed effective process is the *Zwanzig closure*, which ensures that the time-marginals of the reduced process match those of the full dynamics [GKS04]. However, this results in a non-Markovian equation, which is difficult to simulate exactly. Legoll and Lelièvre [LL10] studied an alternative *effective dynamics* Z_t , where

instead of conditioning on the full history of X_t , the evolution of Y_t is conditioned on the invariant measure $\mu = Z^{-1} \exp(-\beta V)$ associated with X_t :

$$dZ_t = b(Z_t) dt + \sqrt{2\beta^{-1} M^{1/2}(Z_t)} dB_t. \quad (5)$$

The drift b , the matrix M and the process B_t are described as follows:

$$b(z) = \mathbb{E}_\mu[\mathcal{L}\xi(X) \mid \xi(X) = z], \quad (6)$$

$$M(z) = \mathbb{E}_\mu[D\xi(X)D\xi(X)^\top \mid \xi(X) = z]. \quad (7)$$

Thus, the effective dynamics $Z_t \in \mathbb{R}^d$ are constructed by conditioning the drift and diffusion of the projected dynamics (2) Y_t by fixing ξ under the measure μ . Z_t is intrinsically low-dimensional and can be simulated using established numerical methods [WV04; Mar+06]. The downside of the effective dynamics is that the laws of Z_t and Y_t do not coincide, so Z_t may obfuscate the statistics of Y_t . Finding error estimates for guaranteeing the proximity of Z_t and Y_t is therefore a highly active topic of research with a number of works [LL10; LLS19; LZ19b; Duo+18; Sha17] exploring the cases arising from different combinations of assumptions on the underlying dynamics X_t , the CV ξ , and ways to measure distances between stochastic processes. In this paper we are concerned with the *scale separating* case of the underlying dynamics where the potential $V := V_\epsilon$ is given by a sum of a *confining potential* $V_1 \geq 0$ and a *driving potential* V_0 . The confining potential is defined so that the level set

$$\mathcal{M} := \{V_1 = 0\} \quad (8)$$

has co-dimension 1 in \mathbb{R}^N . The effect of the confining potential is controlled by the small parameter $\epsilon \ll 1$:

$$V = V_0 + \epsilon^{-1} V_1. \quad (9)$$

Potentials of the form (9) arise routinely in MD simulations where the inter-atomic energy is given by a sum of strong covalent bonds (corresponding to the stiff $\epsilon^{-1} V_1$ term) and weak torsion energies (corresponding to the term V_0). In this scale-separating case, the small parameter ϵ confines X_t to reside near \mathcal{M} , and is henceforth termed the *residence manifold*. On \mathcal{M} , the underlying slow process is directed by the driving potential V_0 . More notably, it is shown in [LL10] that the distance between Z_t and Y_t as measured by relative entropy can be made to scale as $C + O(\epsilon)$ if the following equation, the *orthogonality condition*, is satisfied:

$$D\xi \nabla V_1 = 0. \quad (\text{OC})$$

In a toy two-dimensional example [LL10] demonstrated that designing CVs which satisfied (OC) was instrumental in reproducing residence times via the effective dynamics Z_t . However, most realistic MD simulations are high-dimensional and consist of not one, but several confining potentials at different scales, resulting in complicated residence manifolds of intrinsic dimension significantly smaller than N .

1.1 Aims and contributions

In this paper, we aim to apply the theory of quantitative coarse graining as outlined in [LL10; Duo+18; LZ19b] towards a numerical method for obtaining CVs.

1. We review the theory of quantitative coarse graining from [LL10; Duo+18; LZ19b] and demonstrate how two geometric conditions, the orthogonality condition (OC) and the projected orthogonality condition (POC), emerge as sufficient conditions for reducing the discrepancy between the projected dynamics Y_t (2) and the effective dynamics Z_t (5) as quantified by relative entropy (30) and pathwise distance respectively (33). We evaluate such analytical conditions on CVs in the context of reproduction of reaction rates in molecular dynamics simulations. In particular, we prove that (OC) and (POC) are equivalent (Proposition (2)). Moreover, we provide evidence that the reaction rate can be reproduced even if the diffusion tensor $M(z)$ is rank-deficient. We illustrate this fact for the anti-gauche transition rate in the *normal*-butane molecule C_4H_{10} (henceforth simply referred to as *butane*) (Table (2)).
2. We propose a general procedure for designing CVs based on (OC) (Algorithm (1)). We show how to integrate several tools from manifold learning such as diffusion maps [Coi+08], diffusion nets [Mis+19], group invariance, and independent eigencoordinate selection [CSF19] to learn a neural network-based representation of \mathcal{M} as *hypersurface* (Algorithm (6)). We remark that this hypersurface $\widehat{\mathcal{M}}$, henceforth termed the *surrogate manifold* may contain self-intersections despite the use of functionally independent coordinates. As a solution, we propose a novel manifold learning technique, Laplacian Conformal Autoencoder (LAPCAE) which can *undo* these self-intersections (Figure (10)).
3. We underline the instrumental role played by group invariance in the post-processing of MD data. In particular, we propose mapping, or *featurizing* data sampled from overdamped Langevin dynamics X_t (1) through a feature map \mathcal{F} with invariances to rotations, translations, or reflections. We show (Figure 9) that different feature maps can provide markedly different embeddings of the same data. Moreover, we demonstrate for butane that the positions of the hydrogen atoms are *necessary* for learning accurate representations of the dynamics. This point is of particular interest to the development of MD workflows, where currently it is standard practice to post-process simulation data by discarding coordinates of light atoms.
4. We conduct a detailed investigation of our algorithm on butane as a case study. Although butane is a toy model for studying conformational dynamics, it is nonetheless the simplest MD example that exhibits the characteristics of MD data, such as rotation and translation invariance, low intrinsic dimensionality, metastability, and slow and fast time scales. Moreover, the existence of a clear CV, the dihedral angle, makes it easier to evaluate and benchmark our proposed three-step algorithm. As a lookahead to our results, the CV learned by our algorithm for the feature map **PlaneAlign** reproduces the anti-gauche transition rate in butane with a relative error of nearly 10% while the dihedral angle yields a relative error of 24% (Table (2)).

The code to reproduce our experiments and train our models has been provided at https://github.com/ShashankSule/CV_learning_butane.

1.2 Related work

CV discovery is a thriving interdisciplinary subject at the intersection of probability theory, numerical analysis, biophysics, and, more recently, machine learning. On the theoretical front, since Legoll and Lelievre’s foundational paper proposing the effective dynamics (5), there have been several subsequent theoretical works that have extended the conditioning approach to multidimensional CVs, non-reversible processes, and non-isotropic diffusions. Moreover, these works have addressed distances between Z_t and Y_t as measured by relative entropy, Wasserstein distance, and the pathwise distance [Duo+18; LZ19a; HNS20; HNS20; LLS19]. On the computational side, there is a vast literature on designing CVs for MD simulations, starting with human-designed CVs [Hei+20; OA23; Cho+07; HK20; Alt+08; SP13], data-driven CVs using classical unsupervised learning methods such as diffusion maps [Roh+11; ZRC13; PC14], PCA (and variants) [RA07; GZ07], LDA [SMH23], IsoMap [SK11; Zhe+13], and tICA [MP17; SP15; SG21] or its generalization, the variational approach for conformational (VAC) dynamics [Pér+13; NN13; Nus+14]. With the burgeoning ability to train highly nonlinear deep models, deep learning methods for generalizing the supervised learning methods mentioned above such as VAMPnets [CM19; Mar+18; BPP21] and informational bottlenecked techniques such as time-lagged autoencoders [WN18; ZS23; CF18] or variational autoencoders [WT21; Wan+24a; Rib+18; Her+18] have emerged. The present paper sits at the intersection of theory and application in the sense that it realizes the quantitative coarse-graining theory into an algorithm applied to an MD system. A closely related work towards the same goal is the recent paper [ZS24].

1.3 Organization

The rest of this paper is organized as follows. In Section (2), we review the theory of quantitative coarse-graining from [LL10; Duo+18; LZ19b] where we state relative entropy and pathwise distance estimates for the discrepancy between the projected dynamics and the effective dynamics. In Section (3), we study two conditions emerging from this theory, the orthogonality condition (OC) and the uniform positive definiteness of $D\xi$ (2). We also propose a numerical method for designing neural network-based CVs. The following two sections are more experimental and concern the application of our algorithm to butane. In particular, we describe how to learn the surrogate manifold $\widehat{\mathcal{M}}$ in Section 4 and we learn the CV and present results for transition rate estimation in Section 5.

2 A brief overview of quantitative coarse-graining

2.1 Collective Variables

In this section, we review results from [LL10; Duo+18; LZ19a] to describe how (OC) emerges as a means to optimize coarse-graining error between Z_t (5) and Y_t (2). To begin, we state

some general regularity conditions which ensure the existence of the invariant measure μ and unique solutions to the all-atom dynamics (1) and the effective dynamics (5):

Assumption 1. *We assume the potential V satisfies:*

$$V \in C^\infty(\mathbb{R}^N) \text{ almost everywhere, } \exp(-\beta V) \in L^1(\mathbb{R}^N). \quad (10)$$

Moreover, we assume that the effective drift (6) and the effective diffusion (7) are Lipschitz:

$$\exists L_M, L_b > 0 \text{ such that } |b(z) - b(z')| \leq L_b |z - z'|, \quad \|M(z) - M(z')\|_F \leq L_M |z - z'|. \quad (11)$$

Conditions (10) and (11) ensure that both X_t and Z_t exist and are unique. We note here that [Duo+18] gives a more technical assumption for the CV ξ (see [Duo+18, Eq. (C3)]). However, insofar as we are concerned with relative entropy estimates, this assumption is only used for proving that the effective dynamics have Lipschitz coefficients. Therefore, by assuming the above Lipschitzness we can remove this more technical assumption appearing in [Duo+18]. A more consequential condition for studying the effective dynamics is the boundedness of the singular values of $D\xi D\xi^\top$:

Assumption 2. *We assume that $\xi \in C^3(\mathbb{R}^N)$. Moreover, there exists $\delta_\xi > 0$ such that the collective variable ξ satisfies:*

$$D\xi D\xi^\top \succcurlyeq \delta_\xi^2 I_d \quad (12)$$

Here I_d is a $d \times d$ identity matrix.

Given Assumption 2, the conditioning approach may be further clarified through the use of an integral formulation. First, we introduce the level set $\Sigma_z := \{\xi = z\}$. Since assumption (2) ensures that z is a regular value of ξ , by the implicit function theorem, Σ_z is a smooth manifold of codimension d whose cotangent space is spanned by the rows of the Jacobian $D\xi$. In particular, the level sets $(\Sigma_z)_{z \in \mathbb{R}^d}$ foliate \mathbb{R}^N via:

$$\mathbb{R}^N = \coprod_{z \in \mathbb{R}^d} \Sigma_z. \quad (13)$$

Consequently, the *co-area formula* [EG92] can be used to break up the integral on \mathbb{R}^N into integrals on Σ_z . For instance, if $\varphi : \mathbb{R}^N \rightarrow \mathbb{R}$ is bounded and continuous then

$$\int_{\mathbb{R}^N} \varphi(x) \mu(x) dx = \int_{\mathbb{R}^d} \int_{\Sigma_z} \frac{\varphi(x) \mu(x)}{\det(D\xi D\xi^\top)} d\sigma_{\Sigma_z}(x) dz. \quad (14)$$

Note that if $X \sim \mu$ is a random variable, then so is $Z = \xi(X)$. Then (14) is a geometric description of the tower law

$$\mathbb{E}_\mu[\varphi(X)] = \mathbb{E}[\mathbb{E}[\varphi(X) | Z]]. \quad (15)$$

The manifold Σ_z can then be used to describe the probability densities of random variables after conditioning on the values of ξ . In particular, if X is distributed by the invariant

measure $\mu = Z^{-1} \exp(-\beta V(x))$ then $\xi(X) \in \mathbb{R}^d$ is distributed according to the measure μ^ξ given by

$$\mu^\xi(z) dz = Z^{-1} \int_{\Sigma_z} \frac{\exp(-\beta V(x))}{\sqrt{\det(D\xi D\xi^\top(x))}} d\sigma_{\Sigma_z}(x) dz. \quad (16)$$

Therefore, we can define a new measure on the surface Σ_z given by μ_z :

$$\mu_z(x) dx := N_z^{-1} \frac{Z^{-1} \exp(-\beta V(x))}{\sqrt{\det(D\xi D\xi^\top(x))}} d\sigma_{\Sigma_z}(x), \quad (17)$$

$$N_z = Z^{-1} \int_{\Sigma_z} \frac{\exp(-\beta V(x))}{\sqrt{\det(D\xi D\xi^\top(x))}} d\sigma_{\Sigma_z}(x). \quad (18)$$

The normalization constant N_z is used to define the *free energy*:

$$f(z) = -\beta^{-1} \log N_z. \quad (19)$$

By expressing the free energy as an integral we can also write the derivative of the free energy as an integral. This is formulated in [LL10, Lemma 2.2] and [Duo+18, Lemma 2.4]:

Lemma 1. *The derivative of the free energy $\nabla_z f(z)$, termed the mean force is given by*

$$\nabla_z f(z) = \int_{\Sigma_z} F_z(x) dx, \quad (20)$$

$$F_z(x) = (D\xi D\xi)^\top D\xi \nabla V - \beta^{-1} \nabla \cdot ((D\xi D\xi^\top)^\top D\xi). \quad (21)$$

Here $\nabla \cdot$ is the divergence operator and is applied row-wise when applied to a matrix.

Lemma 1 reveals that the mean force can itself be represented as an integral where the integrand F is the *local mean force*. As we shall see, the local mean force will play a crucial role in designing a strategy for choosing a collective variable.

2.2 Measuring the quality of effective dynamics

Many questions around the quality of the CV ξ boil down to measuring how close the effective dynamics process Z_t is to the coarse-grained process Y_t . As such, there are many ways to quantify the proximity between two stochastic processes, but two particularly fruitful criteria, *relative entropy* and *pathwise convergence*, were given in [LL10; Duo+18; LZ19b]. We first discuss the relative entropy criterion.

2.2.1 Relative entropy

Definition 1 (Relative entropy). *Let ν, η be two probability measures on \mathbb{R}^d which are absolutely continuous with respect to the Lebesgue measure. Then the relative entropy $H(\nu, \eta)$ is given as follows:*

$$H(\nu, \eta) := \begin{cases} \int_{\mathbb{R}^d} \ln\left(\frac{d\nu}{d\eta}\right) d\nu, & \text{if } \nu \ll \eta, \\ +\infty & \text{otherwise.} \end{cases} \quad (22)$$

The relative entropy is related to measuring distances between distributions due to the Csiszar-Kullback inequality:

Proposition 1 (Csiszar-Kullback inequality). *Let $\|\nu - \eta\|_{TV}$ be the total variation distance between the probability measures ν and η on the σ -algebra \mathcal{G} . Then*

$$\|\nu - \eta\|_{TV} := \sup_{A \in \mathcal{G}} |\mu(A) - \nu(A)| \leq \sqrt{2H(\nu, \eta)}. \quad (23)$$

The Csiszar-Kullback inequality shows that reducing relative entropy between distributions is a bona fide way of making two distributions close to each other in the TV norm. This was the content of the main result [LL10] which showed how to reduce the relative entropy between the $\mathcal{P}(Y_t)$ and $\mathcal{P}(Z_t)$ distributions on \mathbb{R}^d induced by Y_t and Z_t . In [Duo+18], this result was generalized for a d -dimensional collective variable where [Duo+18] imposed a few additional assumptions:

Assumption 3. *There exists $\rho > 0$ such that for every probability measure ν satisfying $\nu \ll \mu_z$*

$$H(\nu, \mu_z) \leq \frac{1}{2\rho} \int_{\Sigma_z} \left\| \nabla \ln \left(\frac{d\nu}{d\mu_z} \right) \right\|^2 d\nu. \quad (24)$$

The above inequality is the log-Sobolev inequality and ρ is the log-Sobolev constant.

The log-Sobolev constant determines how quickly a Markov chain mixes to its invariant distribution. In particular, if $\partial_t \mu_t = \mathcal{L}^\dagger \mu_t$ is the Fokker-Planck equation and $\mathcal{L}^\dagger \mu = 0$ is the stationary solution, then by Boltzmann's H-theorem (see e.g. [VW19, Lemma 2]), we have

$$H(\mu_t, \mu) \leq \exp(-2\rho t) H(\mu_0, \mu). \quad (25)$$

If ρ is large, then the associated diffusion process on μ_z mixes quickly. Since Assumption (3) stipulates that every $\mu_z \in \mathbb{R}^d$ shares a single ρ , this implies that processes on Σ_z mix *uniformly quickly*. Next, we turn to an assumption regarding the local mean force F_z in (5). We can endow Σ_z with a geodesic distance:

$$d_z(x_1, x_2) := \inf \left\{ \int_0^1 \|\gamma'(t)\| dt \mid \gamma(0) = x_1, \gamma(1) = x_2, \gamma(t) \in \Sigma_z \right\}. \quad (26)$$

Assumption 4. *We assume that the local mean force is κ -Lipschitz from Σ_z to \mathbb{R}^d as measured by the domain metric d_z and the range metric $\|x - y\|_M^2 = (x - y)^\top M(x - y)$:*

$$\kappa := \sup_{z \in \mathbb{R}^d} \sup_{x_1, x_2 \in \Sigma_z} \frac{\|F_z(x_1) - F_z(x_2)\|_{M(z)}}{d_z(x_1, x_2)} < +\infty, \quad (27)$$

where F_z is the local mean force given by (21).

The last assumption relates to the variation of $D\xi D\xi^\top$ from its mean $M(z)$ (7) on each level set Σ_z .

Assumption 5. Since $D\xi$ is smooth, its restriction to Σ_z is well-defined and is measurable. Let $L(z) : \mathbb{R}^d \rightarrow \mathbb{R}$ be given by

$$L(z) := \|(M(z) - D\xi(x)D\xi(x)^\top)(D\xi(x)D\xi(x)^\top)^{-1/2}\|_{L^\infty(\Sigma_z)}. \quad (28)$$

We assume that

$$\lambda := \|L(z)\|_{L^\infty(\mathbb{R}^d)} < +\infty. \quad (29)$$

The constant λ , in some sense, measures how far ξ is from being an affine function. If, for instance, $\xi = Ax + b$ then $\lambda = 0$ because $D\xi = A$ and $M(z) = AA^\top$.

[LL10] proved the following result which was later generalized by [Duo+18]:

Theorem 1. Let $\mathcal{P}(Z_t), \mathcal{P}(Y_t)$ denote the distributions of Z_t, Y_t and suppose that Z_0 and Y_0 are identically distributed. Under the Assumptions 1, 2, 3, 4, and 5,

$$H(\mathcal{P}(Z_t), \mathcal{P}(Y_t)) \leq \frac{1}{4} \left(\lambda + \frac{\kappa^2 \beta^2}{\rho^2} \right) (H(\mathcal{P}(X_0), \mu) - H(\mathcal{P}(X_t), \mu)). \quad (30)$$

If $D\xi$ is constant on the level set Σ_z then $\lambda = 0$.

The estimate (30) was referred to as an “intermediate time” estimate in [LL10]. The reason is as follows: as $t \rightarrow \infty$, it was shown that the effective and projected dynamics have the same invariant measure given by $\xi_\# \mu$, the pushforward of μ by ξ . Thus, the left-hand side of (30) decays to zero while the right-hand side does not, so the bound is not sharp in the $t \rightarrow \infty$ limit. Moreover, if $t = 0$ then both sides of (30) vanish. Thus, the estimate (30) prescribes control on intermediate $t \in (0, \infty)$.

2.2.2 Reducing the relative entropy and the orthogonality condition

Suppose V satisfies the scale separation condition:

$$V = V_0 + \epsilon^{-1} V_1. \quad (9)$$

In this case, [LL10] computed the local mean force in (21) explicitly [LL10, p. 2150]:

$$F = \frac{2}{\epsilon} \frac{D\xi \nabla V_1}{\|D\xi\|_2^2} + \frac{D\xi \nabla V_0}{\|D\xi\|_2^2} - \beta^{-1} \nabla \cdot \left(\frac{D\xi^\top}{\|D\xi\|_2^2} \right). \quad (31)$$

From now on, we will omit the subscript z from the local mean force for brevity. Since $\epsilon \ll 1$, for a general CV $F = O(1/\epsilon)$ and therefore κ (27) will be $O(1/\epsilon)$. However, if (OC):

$$D\xi \nabla V_1 = 0$$

is satisfied then $F = O(1)$. Moreover, in this case, ρ (24) becomes $O(\epsilon)$ and therefore, the relative entropy estimate reduces to (see [LL10, p. 2150] or [Duo+18, Eq. (4.3)]):

$$H(\mathcal{P}(Z_t), \mathcal{P}(Y_t)) \leq \frac{1}{4} (\lambda + O(\epsilon)) (H(\mathcal{P}(X_0), \mu) - H(\mathcal{P}(X_t), \mu)). \quad (32)$$

2.3 [LL10]'s example

The above calculation shows how (OC) emerges as a way to make the error estimate (30) small. However, it also imparts a geometric requirement to the CV by stipulating that its level sets Σ_z must be orthogonal to those of the confining term V_1 . This was illustrated in [LL10, Table 1] where a toy two-dimensional system with $V = (x^2 - 1)^2 + 100(x^2 + y - 1)^2$ was considered and the quality of the effective dynamics (5) for two CVs, $\xi_1(x, y) = x$ and $\xi_2(x, y) = x \exp(-2y)$, was evaluated. Notably, ξ_2 satisfies (OC) while ξ_1 does not. The effective dynamics under ξ_2 were able to reproduce residence times with a relative error less than 1%, while the effective dynamics under ξ_1 reproduced residence times with 23% relative error (see [LL10, Table 1]). This example suggests that imposing (OC) significantly improves the CV design.

Notably, the approach of using (OC) does not touch the constant λ appearing in the reduced error estimate (32). In fact, λ is seemingly the more significant contributor to the error since it makes the error estimate (32) behave as $O(1)$ irrespective of (OC). It has been noted in [LL10] and [Duo+18] that $\lambda = 0$ if (i) ξ is affine or, more generally, (ii) $D\xi$ is constant on Σ_z for every z . Both conditions (i) and (ii) are rather restrictive. Therefore, there seems to be a geometric trade-off in terms of reducing λ and κ simultaneously. In this paper, guided by [LL10]'s example, we will focus on (OC) exclusively, leaving this fascinating trade-off as the subject of future investigation.

2.3.1 Pathwise estimates

Next, we discuss another criterion for measuring the distance between two stochastic processes: the *pathwise distance* defined as follows:

Definition 2. Let A_t, B_t be two \mathbb{R}^d -valued stochastic processes defined on $t \in [0, T]$ and adapted to the same filtration $(\mathcal{F}_t)_{0 \leq t \leq T}$. Then the pathwise distance between A_t and B_t is given by

$$d(A_t, B_t) := \mathbb{E} \left[\sup_{t \in [0, T]} |A_t - B_t| \right]. \quad (33)$$

Note that two processes with zero pathwise distance induce, for a fixed t , the same distribution on \mathbb{R}^d and therefore have zero relative entropy. The works [LL10; LLO17; LZ19b] describe the conditions under which the projected process (2) and effective dynamics (5) may be brought close in terms of this much stronger distance between stochastic processes. To set up this result, we define the projection operator Π induced by the collective variable:

$$\Pi = I - \sum_{i,j} (\Phi^{-1})_{ij} \nabla \xi_i \nabla \xi_j^\top \quad (34)$$

where $\Phi = D\xi D\xi^\top$. With the projection operator Π , the infinitesimal generator (4) can be decomposed as

$$\mathcal{L} = \mathcal{L}_0 + \mathcal{L}_1 \quad (35)$$

where

$$\mathcal{L}_0 = \frac{e^{\beta V}}{\beta} \sum_{i,j} \delta_{ij} \frac{\partial}{\partial x_i} \left(e^{-\beta V} \Pi_{ij} \frac{\partial}{\partial x_j} \right), \quad (36)$$

$$\mathcal{L}_1 = \frac{e^{\beta V}}{\beta} \sum_{i,j} \delta_{ij} \frac{\partial}{\partial x_i} \left(e^{-\beta V} (I - \Pi)_{ij} \frac{\partial}{\partial x_j} \right). \quad (37)$$

Furthermore, we assume

$$\begin{aligned} \kappa_1^2 &:= \sum_i \int (\Pi \nabla \mathcal{L} \xi_i) \cdot (\Pi \nabla \mathcal{L} \xi_i) d\mu < \infty, \\ \kappa_2^2 &:= \sum_i \int (\Pi \nabla M_{ij}) \cdot (\Pi \nabla M_{ij}) d\mu < \infty. \end{aligned} \quad (38)$$

Next, we state the result of the pathwise distance between the effective dynamics the coarse-grained process below in Theorem 2:

Theorem 2. [LZ19b, Theorem 1] *There exists a constant $\gamma(V, \xi) > 0$ such that:*

$$d(Y_t, Z_t) \leq \frac{3t}{\beta\gamma} \left(\frac{27\kappa_1^2}{2\gamma} + \frac{32\kappa_2^2}{\beta} \right) e^{Lt} \quad (39)$$

where $L = 3L_b^2 + \frac{48L_M^2}{\beta} + 1$. Here L_M, L_b are Lipschitz constants defined in Assumption (1).

2.3.2 Reducing the pathwise distance in the presence of scale separation.

We consider the potential V with the scale separation in the form of equation (9). In [LZ19b] it was shown that the bound in (39) may be made sharper (and in particular $O(\epsilon)$) if the collective variable ξ is chosen to satisfy the *projected orthogonality condition* (POC)

$$(I - \Pi)^\top \nabla V_1 \equiv 0. \quad (\text{POC})$$

The (POC) concerns choosing the rows of the projection $(I - \Pi)$ to be orthogonal to ∇V_1 . Under (POC) and the scale separation condition (9), Theorem 2 can be applied to show that:

$$d(Y_t, Z_t) \leq t \left(\frac{C_1 \epsilon}{K} + \frac{C_2 \epsilon^2}{K^2} \right) e^{Lt} \sim O(\epsilon) \quad (40)$$

Additionally, under (POC) we note

$$\Pi^\top \nabla V = \Pi^\top \nabla V_0 + \frac{1}{\epsilon} \nabla V_1 = O(1/\epsilon), \quad (I - \Pi)^\top \nabla V = (I - \Pi)^\top \nabla V_0. \quad (41)$$

This implies that

$$\text{Operator } \mathcal{L}_0 \text{ contains large coefficients, while } \mathcal{L}_1 \text{ does not.} \quad (42)$$

We term (42) the *coefficient condition* (CC) and remark that (POC) is a special case of (CC). Moreover, in [LZ19b] it was noted that a good choice of collective variable in the most routinely occurring cases of scale separation falls under (CC).

2.3.3 Simulating the effective dynamics

CVs are essential for identifying and replicating the metastable dynamics of the all-atom dynamics (1). In particular, given ξ , we may identify metastable states \tilde{A}, \tilde{B} typically corresponding to the wells of the free energy $f(z)$ (19). We then lift these metastable states to \mathbb{R}^N by defining $A = \xi^{-1}(\tilde{A})$ and $B = \xi^{-1}(\tilde{B})$. A good CV should yield A and B such that the statistics of the rare transitions between A and B in all-atom space \mathbb{R}^N are replicated by the effective dynamics in CV space \mathbb{R}^d . An important statistic is the transition rate ν_{AB} between A and B defined as follows:

$$\nu_{AB} = \lim_{T \rightarrow \infty} \frac{N_{AB}}{T}. \quad (43)$$

Here N_{AB} is the number of transitions made by X_t from A to B observed during the time interval $[0, T]$. Using the framework of transition path theory (TPT)[EV06], the transition rate can be described via the committor function. In particular, the committor q solves the *committor PDE*

$$\begin{cases} \mathcal{L}q(x) = 0, & x \in \Omega_{AB} := \mathcal{M} \setminus (A \cup B), \\ q(x) = 0, & x \in \partial A \\ q(x) = 1, & x \in \partial B. \end{cases} \quad (44)$$

Then, using q , ν_{AB} may be expressed as:

$$\nu_{AB} = \beta^{-1} Z^{-1} \int_{\Omega_{AB}} \|\nabla q(x)\|^2 \exp(-\beta V(x)) dx. \quad (45)$$

Assuming that ξ separates the metastable states A and B , the effective dynamics may be used to numerically calculate ν_{AB} by finding the corresponding transition rate $\tilde{\nu}_{AB}$ for the low-dimensional effective dynamics. Below we describe a numerical method for computing $\tilde{\nu}_{AB}$. Under Assumption 2, the effective dynamics (5) governing Z_t is equivalent to the following dynamics proposed by [Mar+06]:

$$\hat{Z}_t = -(M(\hat{Z}_t) \nabla_z f(\hat{Z}_t) + \beta^{-1} \nabla \cdot M(\hat{Z}_t)) dt + \sqrt{2\beta^{-1}} M(\hat{Z}_t)^{1/2} dW_t. \quad (46)$$

The equivalence between Z_t and \hat{Z}_t has been noted in [LL10] and it makes Z_t easy to simulate by simulating \hat{Z}_t instead. This amounts to computing the diffusion tensor M and the free energy, which can be done using well-known numerical methods [Mar+06; Mül+21; DRP08; FP17; BBP08]. By utilizing M and f , the committor \tilde{q} in collective variables can be computed as the solution to the following elliptic boundary value problem:

$$\begin{cases} \beta^{-1} e^{\beta f(z)} \operatorname{div}(e^{-\beta f(z)} M(z) \nabla \tilde{q}(z)) = 0, & z \in \tilde{\Omega}_{AB}, \\ \tilde{q}(z) = 0, & z \in \tilde{A}, \\ \tilde{q}(z) = 1, & z \in \tilde{B}. \end{cases} \quad (47)$$

Here $\tilde{\Omega}_{AB} := \xi(\mathcal{M}) \setminus (\tilde{A} \cup \tilde{B})$. The transition rate $\tilde{\nu}_{AB}$ in the CV space is given by:

$$\tilde{\nu}_{AB} = \beta^{-1} Z_F^{-1} \int_{\tilde{\Omega}_{AB}} (\nabla \tilde{q})^\top M(z) \nabla \tilde{q} \exp(-\beta f(z)) dz. \quad (48)$$

Computing ν_{AB} involves solving the high-dimensional committor problem (44) followed by high-dimensional numerical integration of (45), which can be unfeasible or undesirable in practice. Instead, we can compute $\tilde{\nu}_{AB}$ by solving the low-dimensional BVP (47) and using the formula (48). The discrepancy between the original transition rate ν_{AB} and the coarse-grained transition rate $\tilde{\nu}_{AB}$ is [ZHS16]:

$$\nu_{AB} \leq \tilde{\nu}_{AB} = \nu_{AB} + \frac{1}{\beta} \int_{\Omega_{AB}} \nabla[q(x) - \tilde{q}(\xi(x))]^\top M(x) \nabla[q(x) - \tilde{q}(\xi(x))] \mu(x) dx. \quad (49)$$

Thus, coarse-graining by a collective variable ξ overestimates the transition rate unless $q(x) \equiv \tilde{q}(\xi(x))$. It was also noted in [ZHS16] that the high-dimensional committor q is the optimal CV. In fact, if $\xi = q$, then the effective dynamics reside in $[0, 1]$. Moreover, for $z \in (0, 1)$, the effective dynamics (5) become driftless with a diffusion coefficient $M(z) = \beta \nu_{AB} \exp(\beta f(z))$. As a consequence, the committor is given by $\tilde{q}(z) = z$. Plugging these into (48), we get $\tilde{\nu}_{AB} = \nu_{AB}$. Thus q reproduces reaction rates *exactly*. However, computing q accurately by solving the high-dimensional PDE (44) is computationally prohibitive. Therefore, different methods are required to design CVs that minimally distort transition rates.

3 Proposed methodology for learning CVs

The theory of quantitative coarse-graining reviewed above provides guidelines for CV design through analytical conditions for ξ under which the error estimates (30) and (33) may hold and be minimized. Two such conditions are given by Assumption (2) which stipulates that $D\xi D\xi^\top$ is uniformly strictly positive definite and, (OC) and (POC) which make error estimates scale with ϵ in the potentials of the form $V = V_0 + \epsilon^{-1}V_1$, as in (9). In this section, we:

1. prove that (OC) and (POC) are equivalent,
2. numerically demonstrate that Assumption 2 is not necessary for the reproduction of transition rates and may be relaxed to the requirement that $\|D\xi\|$ is bounded away from zero, and
3. propose an algorithm based on (OC) for designing CVs for MD data.

3.1 Conditions (OC) and (POC) are equivalent

The theory on pathwise estimates and relative entropy provides two conditions, (OC) and (POC), which may be used to improve the error estimates for effective dynamics and therefore to learn a collective variable. We now show that (OC) and (POC) are actually *equivalent* and therefore the same condition provides simultaneous improvements in two different error metrics.

Proposition 2. *Let ξ be a collective variable and V be given by the decomposition $V = V_0 + \epsilon^{-1}V_1$ as in (9). Then (OC) and (POC) are equivalent.*

Proof. Let $J := D\xi(x)$. Recall that

$$\Phi = (JJ^\top)^{-1}.$$

Then the entries of $I - \Pi$ are:

$$[I - \Pi]_{lk} = \sum_{i,j} (\Phi^{-1})_{ij} (\nabla \xi_i)_l (\nabla \xi_j)_k = J_l^\top \Phi^{-1} J_k, \quad (50)$$

where J_k and J_l are the k th and l th rows of J . Now, let $J = U_r \Sigma_r V_r^\top$ be the truncated SVD of J where r is the rank of J . Then $\Phi = (JJ^\top)^{-1} = U_r (\Sigma_r \Sigma_r^\top)^{-1} U_r^\top$. Moreover, note that we can write each column of J in terms of the columns of U with coefficients from the rows of V . The k th column of J is therefore:

$$J_k = \sum_{\alpha=1}^r \sigma_\alpha v_{\alpha k} u_\alpha. \quad (51)$$

Now we compute:

$$\begin{aligned} \Phi^{-1} J_k &= U_r (\Sigma_r \Sigma_r^\top)^{-1} U_r^\top \sum_{\alpha=1}^r \sigma_\alpha v_{\alpha k} u_\alpha \\ &= \sum_{\alpha=1}^r \sigma_\alpha v_{\alpha k} U_r (\Sigma_r \Sigma_r^\top)^{-1} U_r^\top u_\alpha \\ &= \sum_{\alpha=1}^r \sigma_\alpha v_{\alpha k} u_\alpha \sigma_\alpha^{-2} = \sum_{\alpha=1}^r \sigma_\alpha^{-1} v_{\alpha k} u_\alpha. \end{aligned} \quad (52)$$

Then $[I - \Pi]_{lk}$ is given by:

$$\begin{aligned} [I - \Pi]_{lk} &= J_l^\top \Phi^{-1} J_k = \left(\sum_{\beta=1}^r \sigma_\beta v_{\beta l} u_\beta^\top \sum_{\alpha=1}^r \sigma_\alpha^{-1} v_{\alpha k} u_\alpha \right) \\ &= \left(\sum_{1 \leq \alpha, \beta \leq r} \sigma_\beta v_{\beta l} \sigma_\alpha^{-1} v_{\alpha k} u_\beta^\top u_\alpha \right) = \left(\sum_{1 \leq \alpha \leq r} \sigma_\alpha v_{\alpha l} \sigma_\alpha^{-1} v_{\alpha k} \right) \\ &= \sum_{1 \leq \alpha \leq r} v_{\alpha l} v_{\alpha k} = [V_r V_r^\top]_{lk}. \end{aligned} \quad (53)$$

Thus, $[I - \Pi]_{lk} = [V_r V_r^\top]_{lk}$ so $I - \Pi = V_r V_r^\top$.

Now recall that (OC) states

$$D\xi(x) \nabla V_1(x) = J \nabla V_1 = U_r \Sigma_r V_r^\top \nabla V_1 = 0.$$

Since columns of $U_r \Sigma_r$ are linearly independent, the last equation is equivalent to

$$V_r^\top \nabla V_1 = 0.$$

This, in turn, by the linear independence of columns of V_r , is equivalent to $[I - \Pi] \nabla V_1 = V_r V_r^\top \nabla V_1 = 0$. Thus (OC) is equivalent to (POC). \square

3.2 The diffusion tensor may be rank-deficient but must not vanish

Assumption (2), stating that $D\xi D\xi^\top \succcurlyeq \delta_\xi^2 I_d$ for a positive constant δ_ξ^2 , ensures that the characterization of the conditional expectations through the co-area formula (14) and therefore the measure $\mu^\xi \propto \exp(-\beta f(z))$ is an invariant measure for the effective dynamics (5) which is equivalent to (46) under Assumption (2). However, in the absence of Assumption (2), the diffusion tensor $M(z)$ may vanish, leading to the loss of ergodicity in the free energy dynamics (46). We describe such a case for butane below.

3.2.1 A chain-like butane molecule

The all-atom dynamics of the butane molecule C_4H_{10} in a solvent under high friction can be modeled using (1) with atomic coordinates X_t residing in $\mathbb{R}^{14 \times 3}$ (see Figure 1). Specifically, the process $\theta(X_t)$ largely resides in the anti ($\theta = \pi$) or gauche ($\theta = \pi/3, 5\pi/3$) states (Figure 2) with rare transitions between them. The anti-gauche transition has therefore received considerable attention in molecular dynamics as a small-scale but significant example of torsional transitions and has served as a benchmark example for algorithms seeking to study conformational dynamics in larger biomolecules such as polymer chains. In practice,

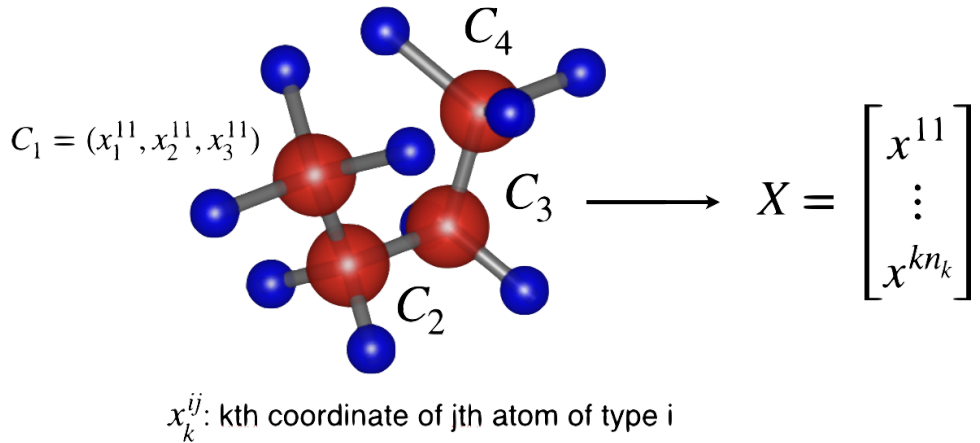


Figure 1: The butane molecule C_4H_{10} can be described in atomic coordinates in \mathbb{R}^{42} .

butane can be coarse-grained along the *dihedral angle* θ in its carbon backbone, where it exhibits metastability. We simulate butane at 300K under Langevin dynamics with high friction, resulting in dynamics well-approximated by the overdamped regime (1). We provide additional details on this approximation in Appendix A where we also describe how the high friction constant should be accommodated for in computing the transition rate via Equation (48). The anti-gauche transition rate obtained via brute-force all-atom simulation is $\nu_{AB} = 1.13 \pm 0.08 \times 10^{-2} \text{ ps}^{-1}$. Now we consider the following three collective variables based on the dihedral angle θ for reproducing the anti-gauche transition rate (Table 1):

1. $\xi_1 = \theta(x)$: The collective variable ξ_1 reproduces the rate as $1.41 \times 10^{-2} \text{ ps}^{-1}$, within 3.5 standard deviations of the reference rate. Notably, the dihedral angle violates

(A) Anti ($\theta = \pi$) (B) Gauche ($\theta = \pi/3, 5\pi/3$) (C) Eclipsed ($\theta = 0$)

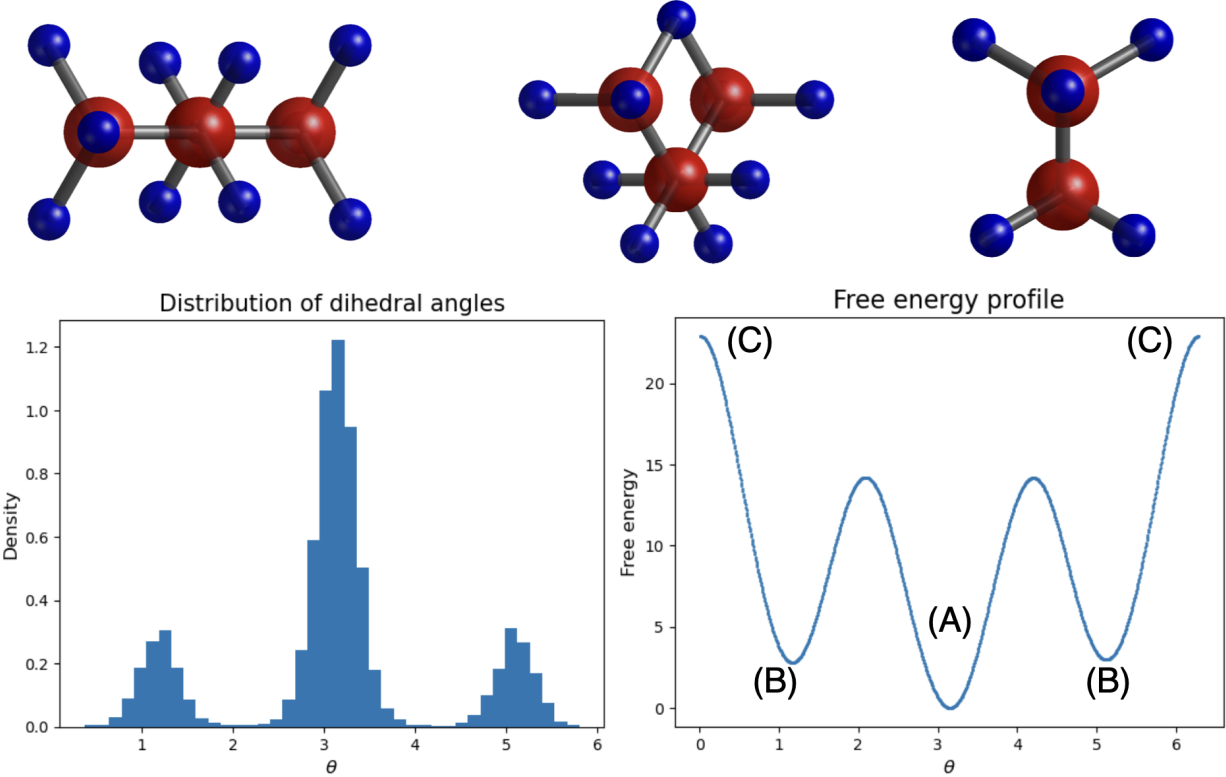


Figure 2: The dynamics of butane can be effectively coarse-grained by the dihedral angle θ . In this case, the free energy f has local minima near the anti and gauche states. Here, the system has been simulated at a temperature of 300 K.

Assumption (2) since it is discontinuous at the point where $\theta = 0$ (i.e the location of the branch cut chosen for the angle).

2. $\xi_2 = \cos \theta(x)$: For the one-dimensional CV ξ_2 resulted in a transition rate of nearly 4.8 standard deviations of the reference rate, at $1.52 \times 10^{-2} \text{ ps}^{-1}$. We posit that this exaggeration occurs because both the free energy F_2 and one-dimensional diffusion tensor A_2 given by equations (19) and (7) vanish (see central panel, Figure 3) leading to both the drift and diffusion terms in the free-energy dynamics (46) to vanish. As a consequence, the dynamics are not irreducible and therefore non-ergodic. Moreover, the chosen gauche configurations form a disjoint set in the atomic dynamics but the CV ξ_2 merges these configurations into one state in the one-dimensional space.
3. $\xi_3 = (\sin \theta(x), \cos \theta(x))$: We observe that for the two-dimensional CV ξ_3 , the diffusion tensor A_3 has rank 1 (see right panel, Figure 3), but the transition rate is reproduced faithfully, at 1.19 ps^{-1} , less than one standard deviation of the reference. This illustrates that Assumption 2 is *not necessary* for a CV to reproduce transition rates. Moreover, ξ_3 preserves the disjoint gauche configurations in CV space, unlike ξ_2 .

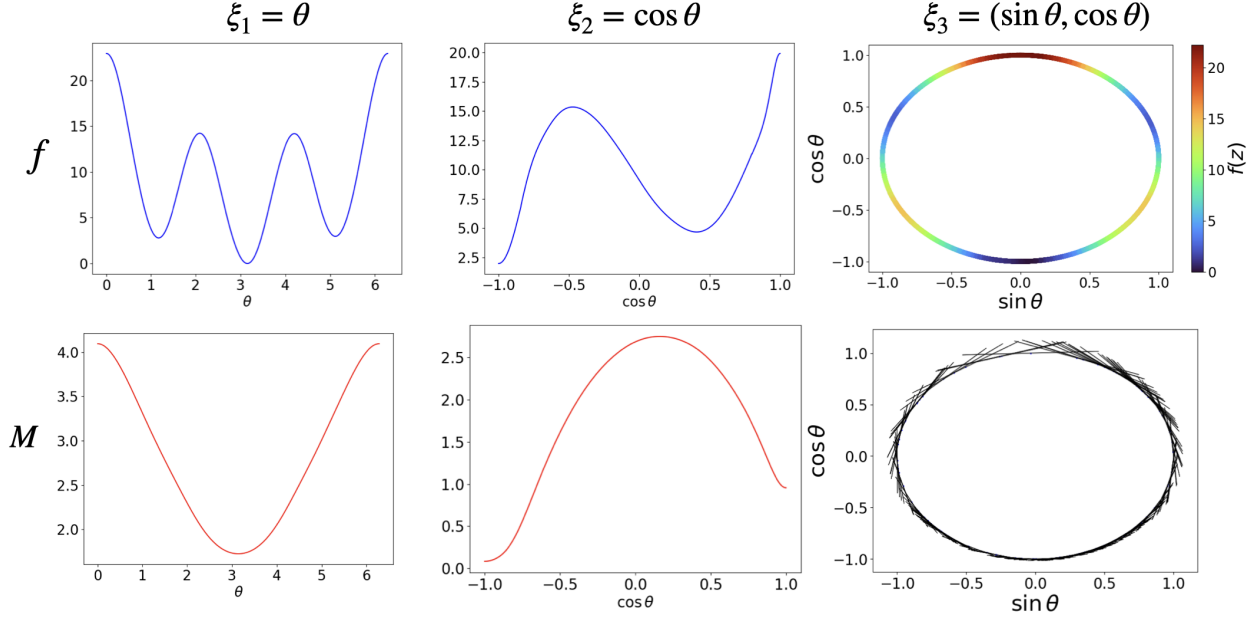


Figure 3: Free energy profiles (top) and diffusion tensors (bottom) for the collective variables based on the dihedral angle (left to right).

Collective variable	Transition rate (ps^{-1})
Reference	$1.13 \pm 0.08 \times 10^{-2}$
Dihedral angle θ	1.41×10^{-2}
$(\sin \theta, \cos \theta)$	1.19×10^{-2}
$\cos \theta$	1.52×10^{-2}

Table 1: Collective variables for butane based on the dihedral angle, and the anti-gauche transition rates they yield.

3.3 Proposed algorithm

In this section, we propose an algorithm for machine-learning CV ξ based on the orthogonality condition (OC). Cautioned from the example in Section (3.2), we aim to ensure that ξ not only preserves metastable states but also observes the condition that $D\xi \neq 0$ for any $x \in \mathcal{M}$. Among the many ways to ensure the non-existence of critical points, a proven effective strategy is to choose ξ to be the encoder in an *autoencoder* [Bel+23]. Additionally, to train such a CV satisfying OC, we would need knowledge of ∇V_1 (the gradient of the confining potential), i.e, the normal vector to the residence manifold \mathcal{M} . However, the key obstruction to this approach is that a priori neither the confining term V_1 in (9) nor the residence manifold \mathcal{M} are known. In this work, we will resolve this obstruction by first obtaining a parameterization $\Psi : \mathbb{R}^N \rightarrow \mathbb{R}^{D+1}$ which projects \mathcal{M} into a D dimensional hypersurface $\widehat{\mathcal{M}} := \Psi(\mathcal{M})$. $\widehat{\mathcal{M}}$ will therefore serve as a surrogate for \mathcal{M} and its property as a hypersurface enables learning a surrogate potential $\widehat{\Phi}$ vanishing on $\widehat{\mathcal{M}}$ with gradients aligned

normally to the $\widehat{\mathcal{M}}$. Finally, we learn $\widehat{\xi}$ which satisfies the (OC) $\nabla\widehat{\xi} \cdot \nabla\widehat{\Phi} = 0$. Notably, this $\widehat{\xi}$ can be *lifted* to an overall collective variable via composition with the parameterization, given by $\xi := \widehat{\xi} \circ \Psi$. Therefore, our method can be described as recovering a CV by enforcing the orthogonality condition in a latent space \mathbb{R}^{D+1} instead of the ambient space \mathbb{R}^N . We summarize our method in Algorithm (1) and elaborate on each step of this method in further sections below.

Algorithm 1: Learning CV that satisfies the orthogonality condition (OC)

Input: Data $\mathcal{X} = \{x_i\}_{i=1}^n \subseteq \mathcal{M}$, invariant density $\mu_i \propto \exp(-\beta V(x_i))$.

Step 1: Learn the residence manifold \mathcal{M} as $\widehat{\mathcal{M}} \subseteq \mathbb{R}^{D+1}$ via a *diffusion map* [CL06] accompanied with a *diffusion net* [Mis+19] learned through Algorithm 6

$$\Psi : \mathcal{M} \rightarrow \widehat{\mathcal{M}} \subseteq \mathbb{R}^{D+1}$$

Step 2: Learn the surrogate potential: Train a neural network

$$\widehat{\Phi} : \mathbb{R}^{D+1} \rightarrow \mathbb{R}$$

such that $\widehat{\Phi}$ vanishes on $\widehat{\mathcal{M}}$.

Step 3: Train an autoencoder where the encoder $\widehat{\xi} : \mathbb{R}^{D+1} \rightarrow \mathbb{R}$ satisfies

$$\nabla\widehat{\xi} \cdot \nabla\widehat{\Phi} = 0$$

Output: Collective variable $\xi = \widehat{\xi} \circ \Psi$.

We remark that Step 1, which involves computing the low-dimensional embedding, is the most technically intricate subroutine of this algorithm. We summarize the subroutine in Algorithm 6 and provide a detailed walkthrough in the section below.

4 Learning the residence manifold

Our goal is to learn a function $\Psi : \mathbb{R}^N \rightarrow \mathbb{R}^{D+1}$ such that \mathcal{M} may be represented by the surrogate manifold $\widehat{\mathcal{M}} = \Psi(\mathcal{M})$. We will learn this map from a trajectory $\mathcal{X} = \{x_i\}_{i=1}^n$ where $x_i \sim X_{i\Delta T}$, i.e the i th point of a time-series simulation of (1). We will adopt diffusion maps [Coi+08] to learn this map Ψ , but this cannot be done straightforwardly on data sampled from the process X_t due to a number of obstacles arising from the nature of MD simulations and the requirements of our proposed algorithm (1). We highlight the key obstacles below:

1. *Group invariance:* In typical MD simulations, the confining potential V_1 is a combination of several strong pairwise energies such as covalent interactions between atoms and is therefore invariant to actions of $\text{SE}(3)$, the group of global translations and rotations of \mathbb{R}^3 (see Definition (3)). Therefore, if $X \in \mathcal{M}$, then $gX \in \mathcal{M}$ where g is a representation of an element in $\text{SE}(3)$. Taking the action over all group elements, the

orbit of any point x under $\text{SE}(3)$ actions forms a submanifold of \mathcal{M} . But this is not the underlying slow direction we would like to discover.

2. *Hypersurface learning*: Since our goal is to learn a normal vector field on $\Psi(\mathcal{M})$, we will learn the residence manifold as a hypersurface (see Definition (6)) in \mathbb{R}^{D+1} . Not every manifold is embeddable as a hypersurface, so we only hope to achieve this hypersurface locally, allowing for possible self-intersections, knots, or lack of orientability. Therefore, we will only attempt to embed the residence manifold as an *immersed* hypersurface.
3. *Out of sample extension*: Typically, manifold learning algorithms will recover a map $\psi : \mathcal{X} \rightarrow \mathbb{R}^{D+1}$. We require that our proposed map Ψ is an extension of ψ to \mathcal{M} .

We surmount the above obstacles as follows:

1. *Group invariance*: To account for $\text{SE}(3)$ invariances, we use *group invariant features* $\mathcal{F} : \mathbb{R}^N \rightarrow \mathbb{R}^{d_{\mathcal{F}}}$ satisfying $\mathcal{F}(x) = \mathcal{F}(gx)$ for all $g \in G$. To use group invariant features, we first project the raw data \mathcal{X} onto a *feature space* by computing a *featurized point cloud* $\mathcal{X}_{\mathcal{F}} := \{\mathcal{F}(x_i)\}$. Assuming that $\mathcal{X}_{\mathcal{F}}$ is sampled from a *featurized manifold* $\mathcal{M}_{\mathcal{F}}$, we compute a diffusion map $\psi_{\mathcal{F}}$ on $\mathcal{X}_{\mathcal{F}}$ instead of \mathcal{X} . We describe our choices of feature map in Section (4.1).
2. *Hypersurface learning*: We apply the diffusion map algorithm to $\mathcal{X}_{\mathcal{F}}$ and obtain $\psi_{\mathcal{F}} : \mathcal{X}_{\mathcal{F}} \rightarrow \mathbb{R}^{D+1}$ such that $\psi_{\mathcal{F}}(\mathcal{X}_{\mathcal{F}})$ appears sampled from a hypersurface immersed in \mathbb{R}^{D+1} . To achieve such an immersion (see Definition (5)) we use independent eigencoordinate selection [CM19].
3. *Out of sample extension*: Once $\psi_{\mathcal{F}}$ has been obtained, we extend it to $\mathcal{M}_{\mathcal{F}}$ via *diffusion nets* [Mis+19], obtaining a neural network $\Psi^{\mathcal{F}}$. The overall parameterization will then be given by $\Psi := \Psi^{\mathcal{F}} \circ \mathcal{F}$.

4.1 Data post-processing matters

We contrast eight different choices of feature maps \mathcal{F} . We will assume $x \in \mathbb{R}^N$ is a point in all-atom space where x is a single vector of all 3D positions of all atoms. This all atom vector may be reshaped into the all-atom matrix $X \in \mathbb{R}^{(N/3) \times 3}$ where the n th row in X is given by $[x_{3n}, x_{3n+1}, x_{3n+2}]$. With this notational change, we describe the feature maps below:

1. No featurization (**NoFeaturization**): $\mathcal{F}(X) = X$.
2. Recentering: Here $\mathcal{F}(X) = X - \mu(X)$, where $\mu(X)$ is the mean of the rows of the atomic coordinates $X \in \mathbb{R}^{14 \times 3}$.
3. Trajectory alignment (**TrajAlign**): Aligning each configuration X_i at time-step t_i to the previous configuration X_{i-1} via Procrustes alignment). **TrajAlign** is a common method for post-processing MD trajectories but it does not correspond to an unambiguous function independent of the data. Consequently, this map is difficult to compute at inference time where a new configuration not in the MD trajectory must be featurized.

4. Computing the gram-matrix of the recentered configurations (GramMatrix): $\mathcal{F}(X) = (X - \mu(X))(X - \mu(X))^\top \in \mathbb{R}^{(N/3) \times (N/3)}$,
5. Computing the gram-matrix of the recentered configurations of the carbon atoms (GramMatrixCarbons): $\mathcal{F}(X) = (MX - \mu(MX))(MX - \mu(MX))^\top \in \mathbb{R}^{4 \times 4}$. Here $M \in \mathbb{R}^{4 \times 14}$ is a *mask* which selects the indices corresponding to the carbon atoms.
6. Global translation of the atoms to realign C_1 to the origin followed by rotation of the $C_1 - C_2$ bond onto the x -axis (BondAlign(1,2)),
7. Global translation of the atoms to realign C_2 to the origin followed by rotation of the $C_2 - C_3$ bond onto the x -axis (BondAlign(2,3)),
8. Changing basis of the recentered configurations such that the C_2, C_3, C_4 atoms all lie in the xy -plane (PlaneAlign).

The above feature maps represent changing levels of group invariances, ranging from no invariance to complete invariance to rotations, reflections, and translations ($E(3)$ invariance). In particular, **TrajAlign** is not a feature map but nonetheless a commonly used pre-processing technique. **NoFeaturization** has no invariance, **Recentering** only has translation invariance, and **GramMatrixCarbons** is only invariant to the actions of $E(3)$ on a subspace of \mathbb{R}^N spanned by the carbon atoms. **BondAlign(1,2)**, **BondAlign(2,3)**, and **PlaneAlign** are $SE(3)$ invariant but not $E(3)$ invariant since they separate antipodal configurations. Finally, **GramMatrix** is $E(3)$ invariant as is well known from Hilbert's classical invariant theory. We visualize **BondAlign(1,2)**, **BondAlign(2,3)**, and **PlaneAlign** in Figures 4, 5, and 6 respectively.

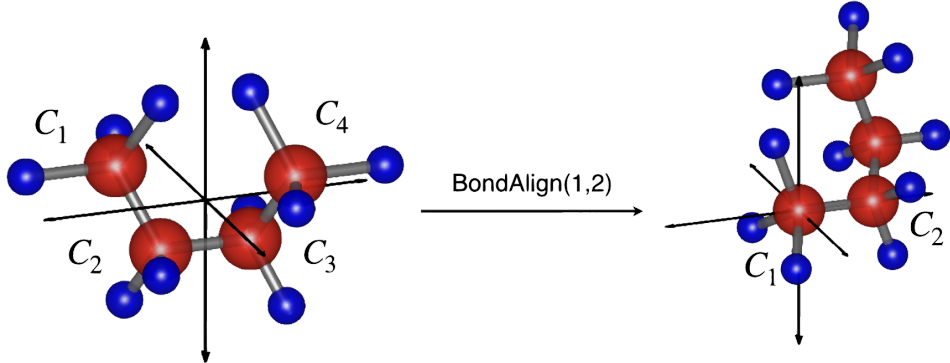


Figure 4: In **BondAlign(1,2)**, the $C_1 - C_2$ bond is aligned along the x -axis.

4.2 Diffusion maps

We pass the data \mathcal{X} through \mathcal{F} to get a featurized pointcloud $\mathcal{X}_{\mathcal{F}} = \{p_i\}$ where $p_i = \mathcal{F}(x_i)$, which we posit is sampled from the featurized manifold $\mathcal{M}_{\mathcal{F}} := \mathcal{F}(\mathcal{M})$. To embed the featurized manifold in low dimensions we use diffusion maps [Coi+08]. Our choice is

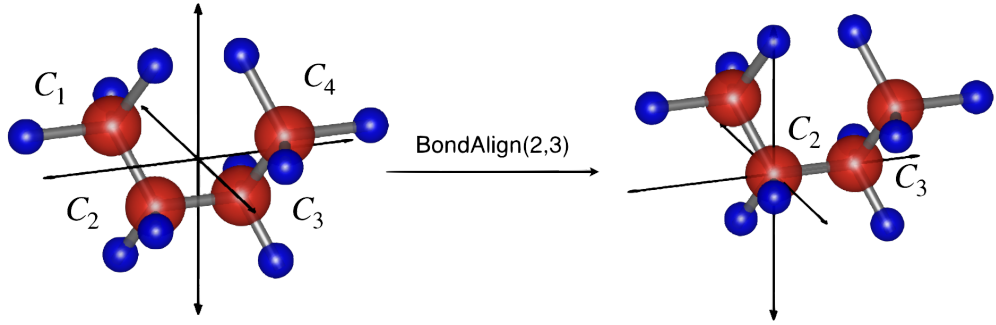


Figure 5: In **BondAlign(2,3)**, the $C_2 - C_3$ bond is aligned along the x -axis.

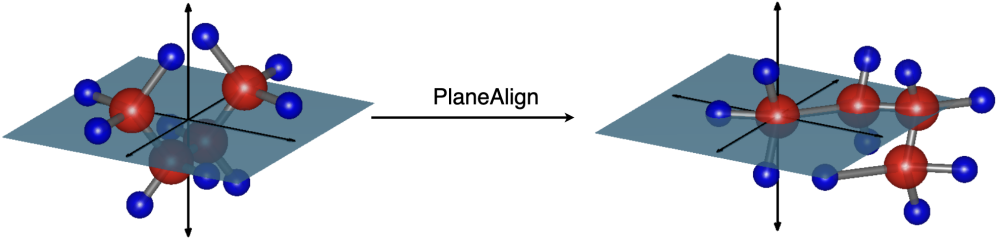


Figure 6: In **PlaneAlign** the basis is changed such that the first three carbon atoms are in the xy -plane.

motivated by the fact that if $\Delta_{\mathcal{M}_F}$ is the Laplace-Beltrami operator on \mathcal{M}_F and $\tilde{\psi}_i$ are the Laplacian eigenfunctions satisfying:

$$-\Delta_{\mathcal{M}_F} \tilde{\psi}_i = \lambda_i \tilde{\psi}_i, \quad (54)$$

then there exists an $m \in \mathbb{N}$ such that the map

$$\tilde{\psi}(x) := (\lambda_1 \tilde{\psi}_1(x), \dots, \lambda_m \tilde{\psi}_m(x)) \in \mathbb{R}^m \quad (55)$$

is an *embedding* [Bat14]. This m can be chosen to be sufficiently larger than the intrinsic dimension $\dim(\mathcal{M}_F)$ of the featurized manifold. The diffusion map $\tilde{\psi}^{n,\epsilon}$ is in turn an approximation of the Laplacian embedding (55) when the density rescaling parameter is set to 1 in the original diffusion map algorithm [Coi+08]. In this setting, $\tilde{\psi}^{n,\epsilon}$ is computed as follows: first, using a Gaussian kernel $k_\epsilon(p, q) = \exp(-\|p - q\|_2^2/\epsilon)$ tuned by a bandwidth ϵ , we form the kernel matrix $K_{ij}^\epsilon = k_\epsilon(p_i, p_j)$ and calculate the kernel density estimate as the vector of its row means:

$$\rho^{n,\epsilon}(i) = \frac{1}{n} \sum_{j=1}^n K_{ij}^\epsilon. \quad (56)$$

Next, we right-normalize the kernel matrix as

$$K^{n,\epsilon} = K_\epsilon [D^{n,\epsilon}]^{-1}, \quad D^{n,\epsilon} = \text{diag}\{\rho^{n,\epsilon}(1), \dots, \rho^{n,\epsilon}(n)\}. \quad (57)$$

The right division by D removes the effect of the sampling density ρ and therefore normalizes the data such that it behaves as though it were sampled via the uniform distribution on $\mathcal{M}_{\mathcal{F}}$. We convert $K_{\epsilon,1}$ into a stochastic matrix of a Markov chain by left-normalizing K_{ϵ} to make its row sums equal to 1:

$$P^{n,\epsilon} = [T^{n,\epsilon}]^{-1} K^{n,\epsilon}, \quad T^{n,\epsilon} = \text{diag}(K^{n,\epsilon} \mathbf{1}_n).$$

Thus, using the kernel k_{ϵ} , we have constructed a Markov chain on the data \mathcal{X} whose transition matrix is given by P_{ϵ} . Then, we form the generator:

$$L^{n,\epsilon} = \frac{1}{\epsilon} (I - P^{n,\epsilon}). \quad (58)$$

Notably, for $f \in C^2(\mathcal{M}_{\mathcal{F}})$ and fixed $p \in \mathcal{M}_{\mathcal{F}}$, let $\mathbf{f} = [f(p_i)]_{p_i \in \mathcal{X}_{\mathcal{F}} \cup \{p\}}$. Then $L^{n,\epsilon} \mathbf{f}(p) \rightarrow \Delta_{\mathcal{M}_{\mathcal{F}}} f(p)$ as $n \rightarrow \infty$ and $\epsilon \rightarrow 0$, so $L^{n,\epsilon}$ is a meshless discretization of $\Delta_{\mathcal{M}_{\mathcal{F}}}$. Moreover, eigenvectors $\tilde{\psi}_j^{n,\epsilon}$ of $L^{n,\epsilon}$ are discretizations of $\tilde{\psi}_j$. Thus, the diffusion map $\tilde{\psi}^{n,\epsilon} : \mathcal{X}_{\mathcal{F}} \rightarrow \mathbb{R}^m$ is given by

$$\tilde{\psi}^{n,\epsilon}(p_i) := \left(\lambda_1^{n,\epsilon} \tilde{\psi}_1^{n,\epsilon}(p_i), \dots, \lambda_m^{n,\epsilon} \tilde{\psi}_m^{n,\epsilon}(p_i) \right). \quad (59)$$

In an abuse of notation we identify the map $\tilde{\psi}^{n,\epsilon}$ with the $n \times m$ matrix formed by stacking the rows $\tilde{\psi}^{n,\epsilon}(p_i)$. We summarize diffusion maps in Algorithm (2).

Algorithm 2: Diffusion Maps

Input: Dataset $\{p_i\}_{i=1}^N \subset \mathbb{R}^{d_{\mathcal{F}}}$, bandwidth $\epsilon > 0$, kernel function $k_{\epsilon}(x, y)$, number of eigenvectors m .

Compute Affinity Matrix

$$K_{ij}^{\epsilon} = k_{\epsilon}(p_i, p_j)$$

Construct KDE

$$\rho^{n,\epsilon}(i) = \frac{1}{n} \sum_{j=1}^n K_{ij}^{\epsilon}.$$

Renormalize kernel

$$K^{n,\epsilon} = K_{\epsilon} [D^{n,\epsilon}]^{-1}, \quad D^{n,\epsilon} = \text{diag}\{\rho^{n,\epsilon}(1), \dots, \rho^{n,\epsilon}(n)\}.$$

Construct Laplacian

$$L^{n,\epsilon} = \frac{1}{\epsilon} (I - P^{n,\epsilon}), \quad P^{n,\epsilon} = [T^{n,\epsilon}]^{-1} K^{n,\epsilon}, \quad T^{n,\epsilon} = \text{diag}(K^{n,\epsilon} \mathbf{1}_n).$$

Construct diffusion map

$$L^{n,\epsilon} \psi^{n,\epsilon} = \Lambda^{n,\epsilon} \psi^{n,\epsilon}$$

Output: Diffusion map embedding $\Lambda^{n,\epsilon} \psi^{n,\epsilon}$

4.3 Independent eigencoordinate selection (IES)

While $\tilde{\psi}^{n,\epsilon}$ approximates the immersion $\tilde{\psi}$ of \mathcal{M}_F in \mathbb{R}^m , this m might be too large for the immersed manifold to be a hypersurface. We will therefore use IES [CM19] to select a subset of columns S of the matrix $\tilde{\psi}^{n,\epsilon}$, $|S| = D + 1$, such that the resulting map

$$\psi_F = (\tilde{\psi}_j^{n,\epsilon}(p))_{j \in S} \quad (60)$$

has rank D . To introduce IES, we need background on differential geometry found in Appendix B. We assume that \mathcal{M}_F is a Riemannian manifold of dimension $\dim(\mathcal{M}_F)$ and metric $\{g(p)\}_{p \in \mathcal{M}_F}$. Let $\tilde{\psi} : \mathcal{M}_F \rightarrow \mathbb{R}^m$ be a smooth immersion and $d\tilde{\psi}_p : T_p \mathcal{M}_F \rightarrow T_{\tilde{\psi}(p)} \mathbb{R}^m$ be its differential at $p \in \mathcal{M}_F$. Note that since $\tilde{\psi}$ is an immersion, $\text{rank}(d\tilde{\psi}) = \dim(\mathcal{M}_F)$. However, $d\tilde{\psi}_p$ may not be full rank since $m \geq \dim(\mathcal{M}_F)$. We can nonetheless compute its pseudo-inverse on vectors in $T_{\tilde{\psi}(p)} \mathbb{R}^m$ to define the *pushforward metric* g_* :

$$\langle u, v \rangle_{g_*} := \langle d\tilde{\psi}_p u, d\tilde{\psi}_p v \rangle_{g(p)}, \quad u, v \in T_{\tilde{\psi}(p)} \mathbb{R}^m. \quad (61)$$

The pushforward metric gives a Riemannian structure to $\tilde{\psi}(\mathcal{M})$ that makes $\tilde{\psi}$ an isometry by definition. In local coordinates in \mathbb{R}^m , this results in a quadratic form at each $\tilde{\psi}(p_i)$:

$$\langle u, v \rangle_{g_*} = u^\top G(p_i) v. \quad (62)$$

Here $G(p_i) \in \mathbb{R}^{m \times m}$ is a local representation of the metric. Crucially, since $\text{rank}(d\tilde{\psi}_p) < m$, $G(p_i)$ will be positive semi-definite with $\text{rank}(G(p_i)) = \dim(\mathcal{M}_F) = D$. Thus, the first D singular vectors of G will span $T_{\tilde{\psi}(p)} \tilde{\psi}(\mathcal{M}_F)$, while the $(D + 1)$ th singular vector will be contained in $T_{\tilde{\psi}(p)} \tilde{\psi}(\mathcal{M}_F)^\perp$. Remarkably, these $G(p_i)$ can be estimated from the data \mathcal{X}_F via Algorithm 3 introduced in [PM13] and named RMetric.

Algorithm 3: RMetric

```

Input : Embedding  $\tilde{\psi}^{n,\epsilon} \in \mathbb{R}^{n \times m}$ , Laplacian  $L^{n,\epsilon}$ , target dimension  $D + 1$ 
for all  $i = 1 \rightarrow n, \alpha = 1 \rightarrow m, \beta = 1 \rightarrow m$  do
     $|\tilde{H}(i)]_{\alpha\beta} = \sum_{j \neq i} L_{ij}^{n,\epsilon} (\tilde{\psi}_\beta^{n,\epsilon}(p_j) - \tilde{\psi}_\beta^{n,\epsilon}(p_i)) (\tilde{\psi}_\alpha^{n,\epsilon}(p_j) - \tilde{\psi}_\alpha^{n,\epsilon}(p_i))$ 
end
for  $i = 1 \rightarrow n$  do
     $|\quad U(i), \Sigma(i) \leftarrow \text{REDUCEDRANKSVD}(\tilde{H}(i), D + 1)$ 
     $|\quad H(i) = U(i) \Sigma(i) U(i)^\top$ 
     $|\quad G(i) = U(i) \Sigma^{-1}(i) U(i)^\top$ 
end
Return:  $G(i), H(i) \in \mathbb{R}^{m \times m}, U(i) \in \mathbb{R}^{m \times (D+1)}, \Sigma(i) \in \mathbb{R}^{(D+1) \times (D+1)}, i \in \{1, 2, \dots, n\}$ 

```

Using RMetric, we compute these singular vectors $U(p_i) \in \mathbb{R}^{m \times (D+1)}$, noting that m is the number of eigenfunctions computed and $D + 1$ is the suggested dimension in which to eventually embed the hypersurface. Intuitively, a D -dimensional hypersurface (locally) has large D -dimensional volume but has small $(D + 1)$ -dimensional volume. Following this intuition, selecting $S \subseteq [m] := \{1, 2, \dots, m\}$ thus amounts to selecting rows of $U(p_i)$ with

large D -dimensional volume but small $(D + 1)$ -dimensional volume. We quantify this in the following way: suppressing the dependence on p_i for a moment, let $U' = U(p_i)[:, [D]]$ be the D column vectors which span $T_{\tilde{\psi}(p_i)}\tilde{\psi}(\mathcal{M}_F)$. Next let $U'_{S'} = U[S', :]$ be a selection of the rows of U' where $|S'| = D$. We consider the log of the volume of the parallelepiped formed by the D -dimensional rows of the column-normalized $U'_{S'}$, written as follows:

$$\text{Vol}(U'_{S'}, p_i) = \log \left(\sqrt{\det \left([U'_{S'}]^\top U'_{S'} \right)} \right) - \sum_{j=1}^D \log \|U'_{S'}[:, j]\|_2^2. \quad (63)$$

To estimate this volume over all points p_i , we take the mean of the normalized projected volume over all the data. Moreover, since S' corresponds to a selection of Laplacian eigenvectors, we also promote selecting eigenvectors with greater smoothness. To do so, we add a regularization term $-\sum_{k \in S'} \lambda_k$ weighted by a parameter ζ which penalizes how much the selected eigenvectors oscillate. Note that we take a minus sign in front since we aim to *maximize* the volume score with the *lowest* frequency eigenfunctions. This leads to the overall score considered in IES [CM19]:

$$R_\zeta(S') = \frac{1}{n} \sum_{i=1}^n \text{Vol}(U'_{S'}, p_i) - \zeta \sum_{k \in S'} \lambda_k. \quad (64)$$

In the original implementation of IES, $R_\zeta(S')$ is maximized over all $S' \subseteq [m]$ with $|S'| = D$ to obtain an optimal set S_* . Here, we simply take $S_* = [D]$, the first D eigenfunctions. This algorithm is summarized in Algorithm 4.

Algorithm 4: Independent eigencoordinate search (IES)

Input : Tangent bundle $\{U'(p_i)\}_{p_i \in \mathcal{X}_F} \subseteq \mathbb{R}^{m \times (D)}$, target dimension $|s| \leq D$, regularization parameter ζ .

for $S' \subseteq [m] : |S'| = s, 1 \in S'$ **do**

$R_\zeta(S') \leftarrow 0$

for $i = 1, \dots, n$ **do**

$U'_{S'} \leftarrow U(p_i)[S', :]$

$R_\zeta(S') \leftarrow$

$R_\zeta(S') + n^{-1} \left[\log \left(\sqrt{\det \left([U'_{S'}]^\top U'_{S'} \right)} \right) - \sum_{j=1}^s \log \|U'_{S'}[:, j]\|_2^2 - \zeta \sum_{k \in S'} \lambda_k \right].$

end

end

$S^* = \text{argmax} R_\zeta(S')$ # Alternative: $S^* = [D]$

Return: Independent eigencoordinates set S^*

Once S^* has been selected, add the next highest frequency eigenfunction to it to form the set of coordinates $S^* \cup k$, but we need to select one more column k of $\tilde{\psi}^{n,\epsilon}$ so that the $(D + 1)$ -dimensional volume is small. Thus, we seek $k \in [m] \setminus S^*$ such that $R_{-\zeta}(S^* \cup \{k\})$ is *minimized*. Note that we change the sign of the penalty term in R at the minimization step to penalize for selecting oscillatory eigenvectors as we did in the maximization step.

Algorithm 5: Hypersurface search (HyperSearch)

Input : Tangent bundle $\{U(p_i)\}_{p_i \in \mathcal{X}_F} \subseteq \mathbb{R}^{m \times (D+1)}$, Optimal D independent coordinates S^* , regularization parameter ζ .

```

for  $k \in [D+1] \setminus S^*$  do
   $S \leftarrow S^* \cup \{k\}$ ,  $R(S, \zeta) \leftarrow 0$ 
  for  $i = 1, \dots, n$  do
     $U_S \leftarrow U(p_i)[S, :]$ 
     $R_{-\zeta}(S) \leftarrow$ 
     $R_{-\zeta}(S) + n^{-1} \left[ \log \left( \sqrt{\det([U_S]^\top U_S)} \right) - \sum_{j=1}^s \log \|U_S[:, j]\|_2^2 + \zeta \sum_{k \in S} \lambda_k \right]$ .
  end
end
 $S \leftarrow \operatorname{argmin} R_{-\zeta}(S)$  # Alternative:  $S = [D+1]$ 
Return: Hypersurface set  $S$ 

```

Algorithm 6: Learning the residence manifold

Input : Featurized data \mathcal{X}_F , kernel bandwidth $\epsilon > 0$, number of eigenvectors m , embedding dimension $D + 1$, regularization parameter ζ .

 $\tilde{\psi}^{\epsilon, n}, L^{n, \epsilon} \leftarrow$ diffusion map $(\mathcal{X}_F, \epsilon, m)$
 $\{U(p_i)\} \leftarrow$ RMetric $(\tilde{\psi}^{\epsilon, n}, L^{n, \epsilon}, D + 1)$
 $S_* \leftarrow$ IES($\{U(p_i)[:, [D]]\}, \zeta$)
 $S \leftarrow$ HyperSearch($\{U(p_i)\}, S_*, \zeta$)
 $\psi_F \leftarrow \psi^{n, \epsilon}[:, S]$
Return: Hypersurface set S , Independent coordinates S_* , Hypersurface embedding ψ_F

We term this addition to IES as Hypersurface Search (HyperSearch) and summarize it in Algorithm 5.

Selecting $D + 1$ and \mathcal{F} . We summarize the entire pipeline for learning the residence manifold in Algorithm 6. The resulting samples $\{\psi_{\mathcal{F}}(p_i)\}$ are assumed to lie on the surrogate manifold $\widehat{\mathcal{M}}$. Clearly, the validity of this algorithm hinges on an appropriate choice of $D + 1$. Ideally, we would like $D + 1 = \dim(\mathcal{M}_{\mathcal{F}}) + 1$, so we may estimate the intrinsic dimension of the featurized pointcloud $\mathcal{X}_{\mathcal{F}}$. Alternately, we can consider the $D + 1$ which provides the best hypersurface immersion for the given data. This can be achieved as follows: we iterate through the values $2 \leq D + 1 \leq m$ and find the $D + 1$ for which the difference between the D -dimensional volume and the $D + 1$ dimensional volume is the largest. This amounts to calculating

$$\text{HyperSurface}(D + 1) := \frac{R_{\zeta}(U'_{S^*}) - R_{-\zeta}(U_S)}{|R_{\zeta}(U'_{S^*})|}. \quad (65)$$

The $D + 1$ that *maximizes* $\text{HyperSurface}(D + 1)$ should be the dimension which provides the best codimension-1 embedding for the data. For simplicity, here we take $S^* = [D]$ and $S = [D + 1]$, motivated by the fact that we are not interested necessarily in independent coordinates but simply by those which form an appropriate hypersurface, i.e. minimizing (65). In Figure 7, we plot $\text{HyperSurface}(D + 1)$ for the feature maps given in Section (4.1).

4.4 Data generation and results on selecting diffusion coordinates

To use Algorithm 6 we first generated a trajectory from an unbiased Langevin dynamics MD simulation of butane with friction coefficient of 10 ps^{-1} at 300K. We collected 10^5 points, each sampled at an interval of 2 femtoseconds. To then determine the best feature map, we subsampled this trajectory at every 100th point to obtain a point cloud of size 10^3 . This was our raw data \mathcal{X} which we then processed through the different feature maps to obtain the featurized point clouds $\mathcal{X}_{\mathcal{F}}$. The parameter ϵ was tuned via the K-sum test in [ECT22]. On each featurized point cloud we ran Algorithm 6, where the number of eigenvectors was chosen to be $m = 25$ and ζ was fixed at 0.01 to penalize the frequencies of the eigenfunctions. Moreover, the parameter ϵ was tuned according to the kernel sum test (see [ECT22]). Figure 7 reveals that, with the **GramMatrixCarbon** feature map, the best hypersurface is obtained when embedding in two dimensions. Additionally, when using **Recentering** or **NoFeaturization**, we require four dimensions to best embed the data with co-dimension 1. We can also flip this analysis and ask: for a given $D + 1$, which feature map \mathcal{F} best embeds the data as a hypersurface? For instance, for both $D + 1 = 2, 3$, the answer is **GramMatrixCarbon**. For $D + 1 = 3$, the next best feature map is **PlaneAlign**. A visual inspection of the 3D coordinates why this is the case: **GramMatrixCarbon** embeds the data as a parabolic sheet (bottom row, fourth column, Figure 9) while **PlaneAlign** embeds as a circular band in 3D (third column, bottom row in Figure 9). However, both can also be embedded in 2D as parabola and a circle respectively (see Figure 8). For **GramMatrixCarbon**, this is observation consistent with the HyperSurface score, where the feature map attains a high score for both $D + 1 = 2, 3$. However, in $D + 1 = 2$, **PlaneAlign** visually embeds as a hypersurface in 2D but *does not* attain a large HyperSurface score. In fact, **PlaneAlign** provides a better embedding

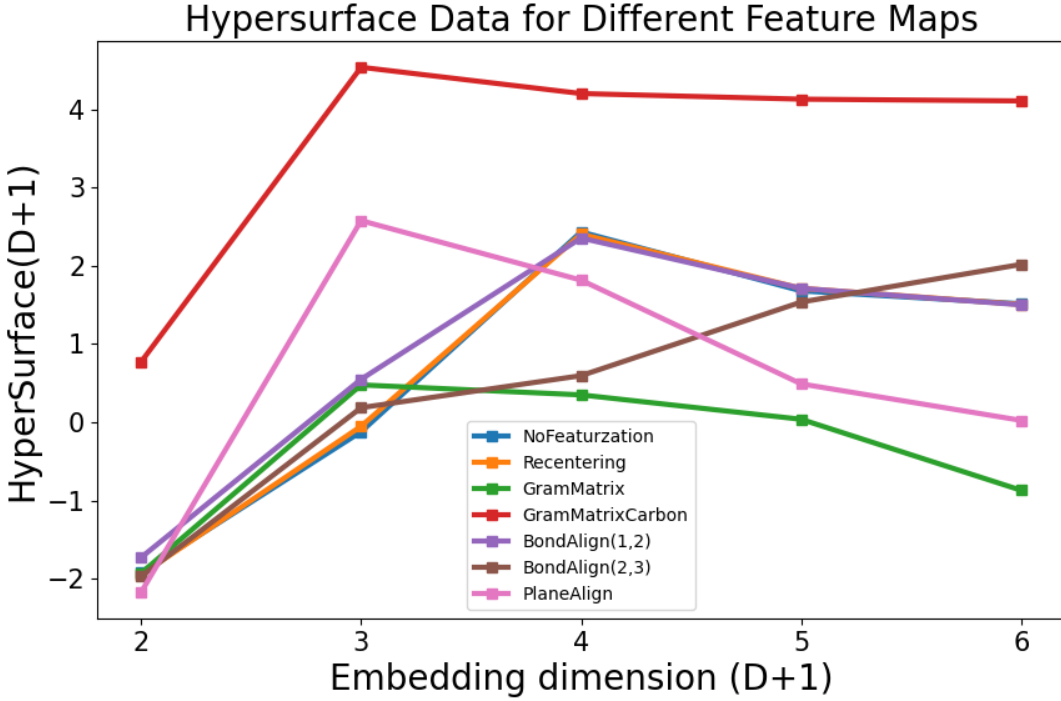


Figure 7: Plotting $\text{HyperSurface}(D + 1)$ against $D + 1$ for different feature maps. Notably, **GramMatrixCarbon** gives the largest value of $\text{HyperSurface}(\cdot)$ at $D + 1 = 2$ which corresponds to the residence manifold of dimension $D = 1$. Moreover **PlaneAlign** seemingly gives the best hypersurface in 3D

than **GramMatrixCarbon** because the **PlaneAlign** embedding is a circle parameterized by the *dihedral angle* while the **GramMatrixCarbon** embedding is a *parabola* parameterized by $\cos \theta$. This analysis reveals the inherent limitations of HyperSurface —it is only a heuristic and can identify critical dimensions for a feature map. However, it can lead to *false negatives*, as in the case of **PlaneAlign** which attains the lowest score for $D + 1 = 2$, but is clearly visually the “best” 2D embedding.

For $D + 1 = 3$, after **PlaneAlign**, **GramMatrixCarbon**, **BondAlign(1,2)** and **GramMatrix** attain the next top 3 scores respectively. The embeddings into 3D are shown in Figure 9. Rather intriguingly, **GramMatrixCarbon** is both embedded as a parabola in two dimensions and as a parabolic sheet in three dimensions. Moreover, the **BondAlign(1,2)** embedding is a paraboloid in 2D (second row, second column) and the **GramMatrix** embedding seems to resemble a wedge product of circles (first row, fourth column).

Importance of hydrogen atoms A highly significant aspect of this analysis is the importance of the hydrogen atoms—the embedding obtained via **GramMatrixCarbon** is parameterized by the $\cos \theta$, which is a somewhat suboptimal collective variable in reproducing transition rates (Table 1). However, in **GramMatrix** when we also include the pairwise inner products with hydrogen atoms, we find that the embedding is smoothly parameterized by θ , where the two disjoint gauche states can be separated.

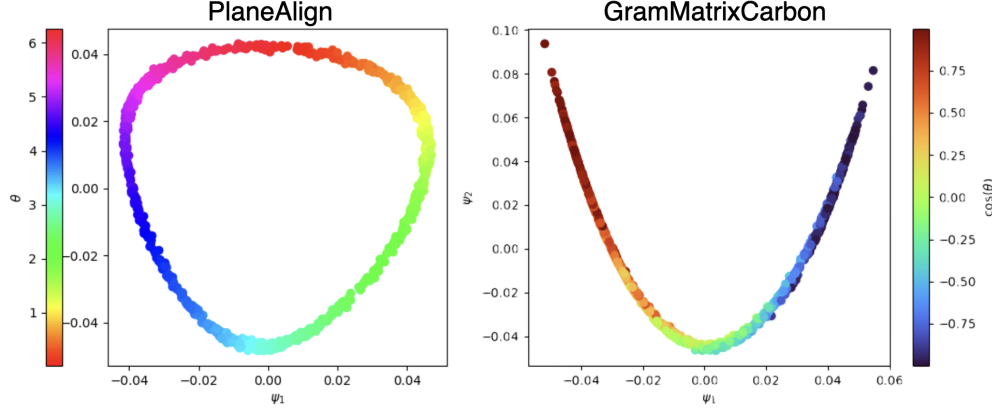


Figure 8: Visualizing the first two selected Laplacian eigenvectors for PlaneAlign and GramMatrixCarbon. Both embeddings form hypersurfaces in two dimensions.

4.5 Diffusion net

After computing the embedding $\psi_{\mathcal{F}}$, we consider the elements of the pointcloud $\{\psi_{\mathcal{F}}(p_i)\}$ as the evaluations of a diffusion net $\Psi_{W_1} : \mathbb{R}^N \rightarrow \mathbb{R}^{D+1}$ where $\Psi_{W_1} = \Psi_{W_1}^{\mathcal{F}} \circ \mathcal{F}$ as a neural network with parameters W_1 (the subscript 1 corresponding to Step 1 of Algorithm (1)). We train $\Psi^{\mathcal{F}}$ such that (1) $\Psi^{\mathcal{F}}$ matches $\psi_{\mathcal{F}}$ at every point $p_i = \mathcal{F}(x_i)$ and (2) $[\Psi_{W_1}^{\mathcal{F}}]_j$, the j th coordinate of $\Psi^{\mathcal{F}}$ is a Laplacian eigenfunction with eigenvalue λ_j . The training objective (1) can be attained by simple mean squared error loss. To achieve training objective (2), we abuse notation and denote $[\Psi_{W_1}^{\mathcal{F}}]_j$ as the evaluations of $[\Psi_{W_1}^{\mathcal{F}}]_j$ on all points p_i . Then the vector $L_{n,\epsilon}[\Psi_{W_1}^{\mathcal{F}}]_j$ represents the action of the Laplacian on this function. Objective (2) stipulates that $L_{n,\epsilon}[\Psi_{W_1}^{\mathcal{F}}]_j(p_i) \approx \lambda_j^{n,\epsilon}[\Psi_{W_1}^{\mathcal{F}}]_j(p_i)$. This reasoning leads to the following loss function proposed in [Mis+19]:

$$\mathcal{L}_{\text{DNet}}(W_1) := \frac{1}{n} \sum_{i=1}^n \|\Psi_{W_1}^{\mathcal{F}}(x_i) - \psi_{\mathcal{F}}(p_i)\|_2^2 + \alpha_{\text{DNet}} \frac{1}{n} \sum_{i=1}^n \sum_{j=1}^{D+1} |L_{n,\epsilon}[\Psi_{W_1}^{\mathcal{F}}]_j(p_i) - \lambda_j^{n,\epsilon}[\Psi_{W_1}^{\mathcal{F}}]_j|^2 \quad (66)$$

We can also train a decoder Ψ_{Dec} but since \mathcal{F} is not injective, we can only carry $\Psi(x_i)$ back to $\mathcal{F}(x_i)$. In this case, the decoder is trained with the following reconstruction loss:

$$L_{\text{DNet}}^{\text{Dec}}[W_1^{\text{Dec}}, W_1] := \frac{1}{n} \sum_{i=1}^n \|\Psi^{\text{Dec}} \circ \Psi(x_i) - \mathcal{F}(x_i)\|_2^2. \quad (67)$$

Here our focus remains on the encoder Ψ .

4.6 Undoing spurious topological features.

Among the SE(3)-invariant feature maps, only BondAlign(2,3) presents a manifold that cannot be embedded as a hypersurface in either two or three dimensions (Figure 9, second row, first column). However, the dihedral angle still seems to smoothly parameterize points on

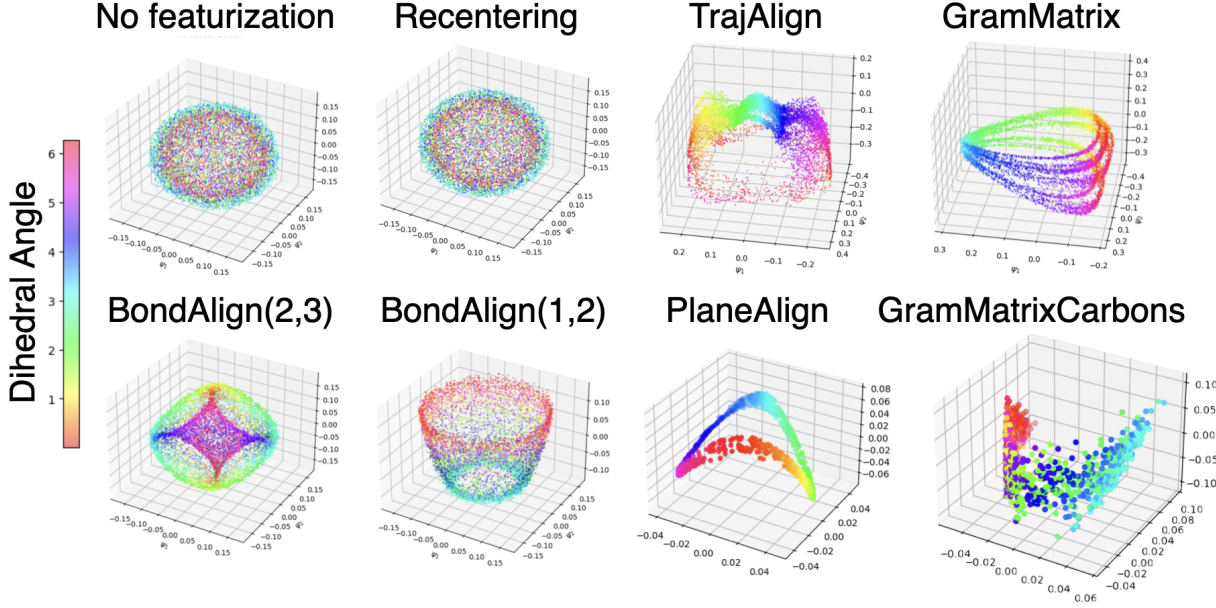


Figure 9: Left to right, top to bottom: The diffusion map embeddings $\{\psi(\mathcal{F}_k(x_i)\}_{x_i \in \mathcal{X}}$ for eight different choices of feature maps with varying degrees of invariance. The points are coloured according to the dihedral angle.

the embedding, which resembles a sphere with handles. We find that this phenomenon persists when applying diffusion maps to data pre-processed via **BondAlign(2,3)** only on the carbon atoms (see top left, Fig. 10). A further look by slicing the embedding at various z -coordinates at this embedding reveals *self-intersections* in three dimensions (see top right, Fig 10). We additionally embed the data post-processed by the feature map **BondAlign(2,3)** into four dimensions and visualize its sliced data in three dimensions with the third coordinate being the *fourth* Laplacian eigenfunction ψ_4 in the bottom left of Fig 10. This reveals that the self-intersections are actually spurious and that the three-dimensional sliced data forms *loops* which can be parameterized using the dihedral angle. This suggests that there is a functional dependence among the first four coordinates $\psi = (\psi_1, \dots, \psi_4)$. We quantify this functional dependence via the following energy proposed in [Kev+24]:

$$\mathcal{E}(\Psi) := \sum_{i < j} |\langle \nabla_{\mathbb{R}^{d_{\mathcal{F}}} \Psi_i, \nabla_{\mathbb{R}^{d_{\mathcal{F}}} \Psi_j} \rangle|^2. \quad (68)$$

The functional (68) was suggested as a regularization term in a *conformal autoencoder*. We now compute a map $\Psi : \mathbb{R}^{14 \times 3} \rightarrow \mathbb{R}^{D+1}$ as a neural network trained to be a conformal autoencoder whose coordinates are Laplacian eigenfunctions. In particular, the encoder is trained to minimize the following loss function:

$$L_{\text{LAPCAE}}^{\text{Enc}}[W_1] := \frac{1}{n} \sum_{i=1}^n \sum_{j=1}^{D+1} |L^{n,\epsilon} \Psi_{W_1}^{\mathcal{F}}(p_i) - \lambda_j^{n,\epsilon} \Psi_{W_1}^{\mathcal{F}}(p_i)|^2 + \alpha_{\text{LAPCAE}} \mathcal{E}(\Psi_{W_1}). \quad (69)$$

We train the overall autoencoder $\Psi^{\text{Dec}} \circ \Psi$ with a weighted combination of $L_{\text{DNet}}^{\text{Dec}}$ (67) and $L_{\text{LAPCAE}}^{\text{Enc}}$ (69):

$$L_{\text{LAPCAE}}[W_1^{\text{Dec}}, W_1] := L_{\text{DNet}}^{\text{Dec}}[W_1^{\text{Dec}}] + \alpha_{\text{LAPCAE}}^{\text{Enc}} L_{\text{LAPCAE}}^{\text{Enc}}[W_1]. \quad (70)$$

After training Ψ on (70) we project the all-atom data to obtain a low-dimensional embedding formed by points $\{\Psi^{\mathcal{F}}(p_i)\}_{i=1}^n$ (bottom left, Fig (10)). Remarkably, the LAPCAE removes the self-intersections, resulting in a cylinder embedded in three dimensions. Moreover, the points are smoothly organized by the dihedral angle. Undoing topological features like spurious knots is an important challenge in data visualization and manifold learning. Our result is therefore of independent interest to geometric data science in addition to the MD community.

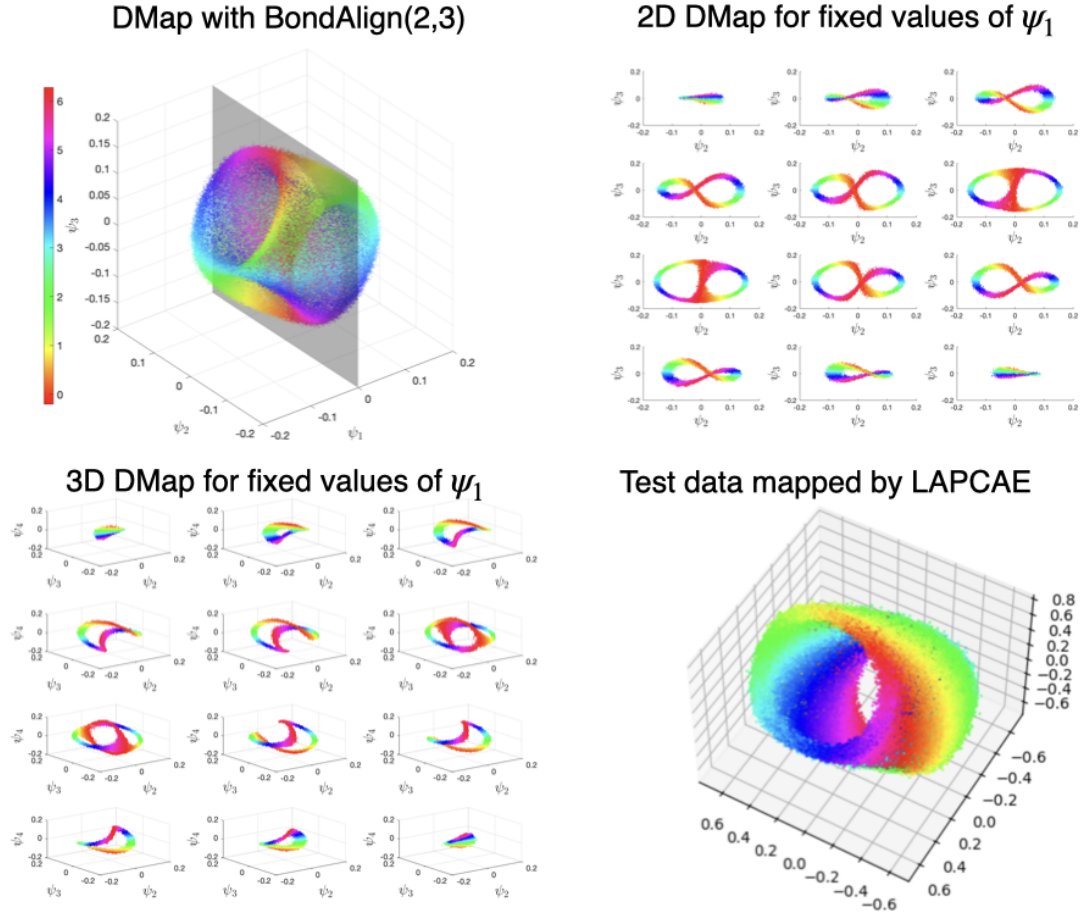


Figure 10: Top left: The diffusion map embedding after featurization by recentering the $C_2 - C_3$ bond on the x -axis. Top right: Slices of the embedding by planes parallel to the xy -plane. Bottom left: Visualizing the sliced data along with the corresponding fourth eigenfunction. Bottom right: The corrected embedding after mapping via a Laplacian conformal autoencoder.

4.7 Computational details

After acquiring hypersurface coordinates for each feature map, we took every 10th point of our overall trajectory $\{X_{i\Delta t}\}_{i=1}^{10^5}$ as a training set \mathcal{X} of size 10^4 . The rest of the points were considered part of the testing set. We then postprocessed this point cloud \mathcal{X} using the group invariant feature maps described in Section (4.1) to obtain featurized pointclouds $\mathcal{X}_{\mathcal{F}}$ and computed the diffusion map on the selected hypersurface coordinates. We then trained a diffusion net with encoder Ψ and decoder Ψ^{Dec} . Both encoders and decoders were four-layer fully connected networks with either \tanh or $x + \sin^2(x)$ activation. We trained these using an ADAM optimizer with learning rate 0.01. For training LAPCAE with the feature map BondAlign applied to the carbon atoms, the constant α_{DNet} , $\alpha_{\text{LAPCAE}}^{\text{Enc}}$ were chosen to be 1.0. We provide additional details regarding neural network training in Appendix C.

5 Learning CVs from the residence manifold

5.1 Learning the confining potential V_1

We assume now that the diffusion net Ψ has been trained and that the data $\hat{\mathcal{X}} = \{y_i\}$ lies on the surrogate manifold $\hat{\mathcal{M}}$ where $y_i = \Psi(x_i)$. Now we aim to learn a surrogate potential $\hat{\Phi}$ which vanishes exactly on $\hat{\mathcal{M}}$. We are aided by the fact that $\hat{\mathcal{M}}$ can be presented as a hypersurface. In this case, a loss for learning $\hat{\Phi}$ may be derived using the eikonal equation. In particular, $\hat{\mathcal{M}}$ may be exhibited (possibly locally) as the boundary of some open set in \mathbb{R}^{D+1} . In this case, then the signed distance function (SDF) $\hat{\Phi}_{\text{SDF}}$ to this open set satisfies $\|\nabla \hat{\Phi}_{\text{SDF}}\|^2 = 1$. We propose that this SDF be a representation of the desired surrogate potential $\hat{\Phi}$. This is because $\nabla \hat{\Phi}_{\text{SDF}}(y) = -N(y)$ where $N(y)$ is the outward pointing normal vector to $\hat{\mathcal{M}}$ at y , i.e the condition we want the surrogate potential $\hat{\Phi}$ to satisfy. A loss function for Φ_{W_2} is given by:

$$L_{\text{eikonal}}[W_2] := \frac{1}{n} \sum_{i=1}^n (\|\nabla \Phi_{W_2}(y_i)\|_2^2 - 1)^2 + \alpha_{\text{zero}} \|\Phi_{W_2}(y_i)\|_2^2. \quad (71)$$

As an alternate approach, given the point cloud $\hat{\mathcal{X}}$, the normals at each point $N(y_i)$ may be estimated directly without needing a neural network by taking a neighborhood of y_i and fitting a tangent plane to this neighborhood. The estimated normal n_i at y_i is then the normal vector to this tangent plane. This method is summarized in algorithm (7).

Algorithm 7: Estimate Normals via k-NN and Tangent Plane Fitting

Input: Point cloud $\widehat{\mathcal{X}} = \{y_i\}_{i=1}^N \subseteq \mathbb{R}^{D+1}$, number of neighbors k

Output: Estimated normals $\{n_i\}_{i=1}^N$

Build a spatial index (e.g., KD-tree) for fast nearest-neighbor queries

foreach $y_i \in \mathcal{P}$ **do**

 Find the k nearest neighbors of y_i : $\{y_j\}_{j=1}^k \leftarrow \text{knn}(y_i, k)$

 Compute the centroid of neighbors:

$$\bar{y} \leftarrow \frac{1}{k} \sum_{j=1}^k y_j$$

 Center the neighbors:

$$Y \leftarrow [y_j - \bar{y}]_{j=1}^k$$

 Compute the covariance matrix:

$$C \leftarrow \frac{1}{k} Y^\top Y$$

 Perform eigen-decomposition or SVD of C to get eigenvalues $\lambda_1 \leq \dots \leq \lambda_d$ and eigenvectors v_1, \dots, v_d

 Assign the normal vector corresponding to the eigenvector with the smallest eigenvalue:

$$n_i \leftarrow v_1$$

end

return $\{n_i\}_{i=1}^N$

After estimating the point cloud normals $\{n_i\} \subseteq \mathbb{R}^{D+1}$ we use these to supplement L_{eikonal} with an additional regularization term to aid learning the surrogate potential Φ . Thus, the final loss for learning Φ is given by:

$$L_{\text{potential}}[W_2] := L_{\text{eikonal}}[W_2] + \frac{\alpha_{\text{normals}}}{n} \sum_{i=1}^n \|\nabla \Phi_{W_2}(y_i) - n_i\|_2^2. \quad (72)$$

Here $\alpha_{\text{normals}} > 0$ is a hyperparameter. In Figure 11 we present $\nabla \widehat{V}$ learned for the **BondAlign(1,2)**, **BondAlign(2,3)**, and **PlaneAlign** feature maps, confirming that the gradients of $\widehat{\Phi}$ are normal to the learned manifold $\widehat{\mathcal{M}}$.

5.2 Learning collective variable ξ

After acquiring the surrogate potential $\widehat{\Phi}$ that vanishes on the surrogate manifold $\widehat{\mathcal{M}}$, we finally train the collective variable $\widehat{\xi}_{W_3}$, given by another neural network with parameters W_3 trained to satisfy the orthogonality criterion with respect to $\widehat{\Phi}$. We will proceed to learn CVs following Algorithm 1 only for the two most promising featurizations, **BondAlign(2,3)** and **PlaneAlign**. To do so, we consider the surrogate potential $\widehat{\Phi}$ obtained by minimizing

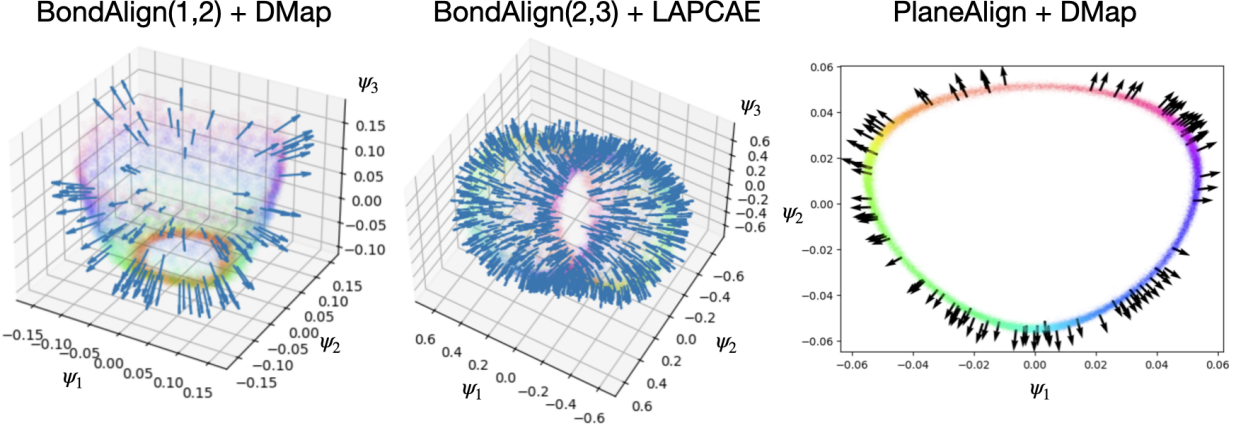


Figure 11: Gradients of potential $\nabla \widehat{\Phi}$ learned for BondAlign(1,2), BondAlign(2,3) and PlaneAlign. Here $\widehat{\Phi}$ is learned by minimizing $L_{\text{potential}}$.

$L_{\text{potential}}$ in (72). In this case $\widehat{\Phi} \approx \widehat{\Phi}_{\text{SDF}}$. However,

$$H\widehat{\Phi}_{\text{SDF}}\nabla\widehat{\Phi}_{\text{SDF}} = 0, \quad (73)$$

where $H\widehat{\Phi}_{\text{SDF}}$ is the Hessian of the signed distance function. Since $\nabla\widehat{\Phi}$ is the normal vector to \mathcal{M} , this implies that the rows of $H\widehat{\Phi}$ given by $\nabla\partial_i\widehat{\Phi}$ satisfy the orthogonality condition (OC). Therefore, $\partial_i\widehat{\Phi}$ may be directly used as a collective variable; alternately, a separate encoder $\widehat{\xi}$ may be trained such that the *normalized gradients* of $\widehat{\xi}$ given by $\nabla\widehat{\xi}/\|\nabla\widehat{\xi}\|$ are aligned with the normalized $\nabla\partial_i\widehat{\Phi}$. One way to avoid dividing by $\|\nabla\widehat{\xi}\|$ is to observe that the Cauchy-Schwarz inequality $|\langle \nabla\widehat{\xi}, \nabla\partial_i\widehat{\Phi} \rangle|^2 \leq \|\nabla\widehat{\xi}\|^2 \|\nabla\partial_i\widehat{\Phi}\|^2$ is an equality if and only if $\nabla\widehat{\xi}$ and $\nabla\partial_i\widehat{\Phi}$ are parallel. Therefore, a loss function for learning $\widehat{\xi}$ is given by:

$$L_{\text{alignment}}[W_3] = \sum_{i=1}^n \|y_i - \xi_{\text{Dec}} \circ \xi(y_i)\|_2^2 + \alpha_{\text{OC}}(|\langle \nabla\widehat{\xi}, \nabla\partial_i\widehat{\Phi} \rangle|^2 - \|\nabla\widehat{\xi}\|^2 \|\nabla\partial_i\widehat{\Phi}\|^2)^2. \quad (74)$$

In Figure 12, we visualize the gradients of $\widehat{\xi}$ for the feature maps BondAlign(2,3) and PlaneAlign which are orthogonal to the surrogate potential $\widehat{\Phi}$ on the learned manifold $\widehat{\mathcal{M}}$. For BondAlign(2,3), we use the loss $L_{\text{alignment}}$ (74) with $\partial_1\widehat{\Phi}$, where $\widehat{\Phi}$ is learned by minimizing L_{eikonal} . For PlaneAlign, we find that $\widehat{\xi}(x) = \text{arctan2}(x_2, x_1)$ (arctan2 returns angle from $-\pi$ to π) is orthogonal to $\nabla\widehat{\Phi}$ and therefore satisfies (OC). Thus, given an interpretable enough visualization, CVs may be devised by inspection. Interestingly, the CV learned via PlaneAlign correlates significantly with the dihedral angle.

5.3 Computational details

For both PlaneAlign and BondAlign(2,3), $\widehat{\Phi}$ and $\widehat{\xi}$ were taken to be four-layer fully connected networks with arctan and $x + \sin^2(x)$ activations respectively. The use of such nonstandard activations was motivated by the spherical/toroidal structure of the surrogate manifolds and the modeling of $\widehat{\Phi}$ as a *signed* distance. The exact architectures and training details have been provided in Table (3) in Appendix C.

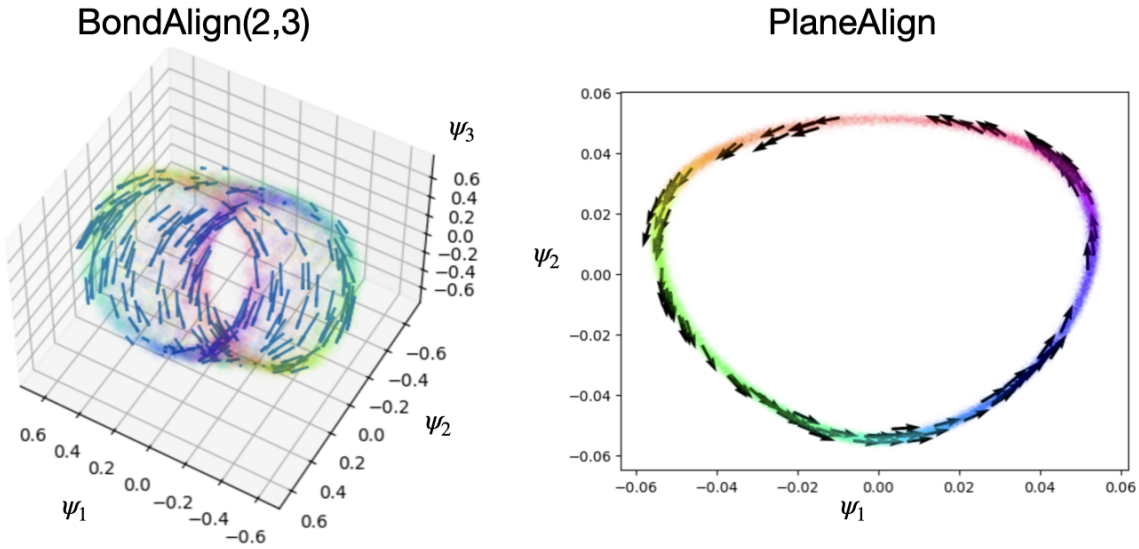


Figure 12: Gradients of CVs for BondAlign(2,3) and PlaneAlign.

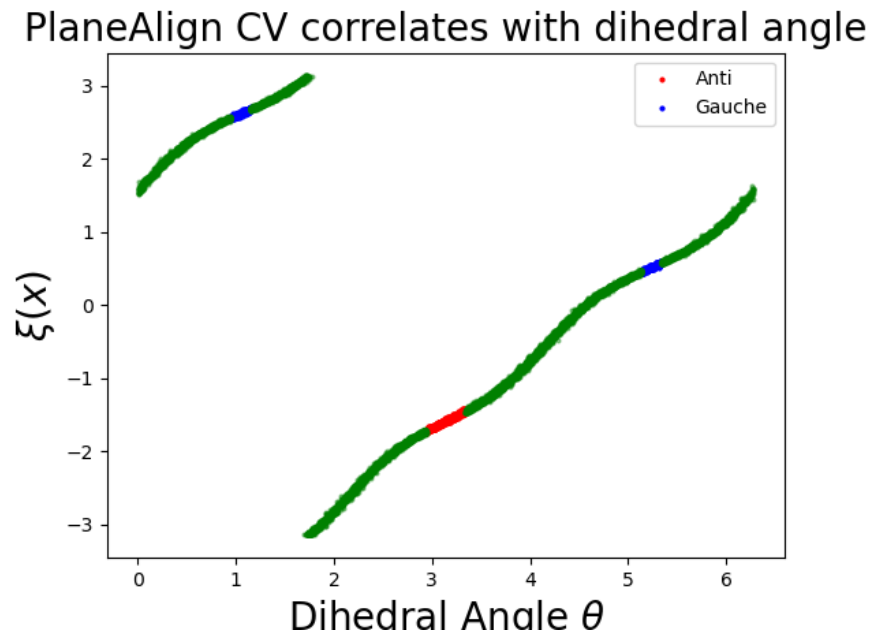


Figure 13: We visualize $(\theta(x_i), \xi(x_i))$ for $x_i \in \mathcal{X}$, the training data used for learning ξ . Note that ξ is a nonlinear function of θ —the single discontinuity is due to the use of the $\arctan 2$ function which requires a branch cut at $\theta = 2\pi$.

5.4 Reproducing transition rates

Using CVs $\xi := \hat{\xi} \circ \Psi$ learned from Algorithm 1 we now reproduce the transition rate ν_{AB} for the anti-gauche transition from the set

$$A = \{|\theta - \pi| \leq 0.2\} \quad \text{to} \quad B = \{|\theta - \pi/3| \leq 0.1\} \sqcup \{|\theta - 5\pi/3| \leq 0.1\}.$$

We will do so by computing $\tilde{\nu}_{AB}$ via (48). This necessitates computing the free energy f and the diffusion tensor $M(z)$. We compute f via *well-tempered metadynamics* [BBP08] and M via the spring force method [Mar+06] respectively.

Our results are presented in Table 2, where we organize the machine-learned collective variables (ML CVs) by the underlying feature map. We find that although the **BondAlign(2,3)** feature map results in a coherent manifold, the CVs learned using such a manifold do not separate the metastable states A and B (see Figure 14). However, the CV learned using **PlaneAlign** corresponds nearly exactly to the dihedral angle, and therefore separates metastable states. In CV space these are identified with the following intervals:

$$A = [-1.75, -1.41], \quad B = [0.43, 0.60] \sqcup [2.54, 2.71]. \quad (75)$$

Using these and applying formula (48) led to a transition rate with less than ten percent relative error. The free energy and diffusion tensors used for computing the transition rates are provided in Figure (6). For completeness, we visualize the free energy landscape and diffusion tensors for the two-dimensional CV learned using **BondAlign(2,3)** in Figure 15 even though we do not compute the anti-gauche transition rate using this CV. Notably the diffusion tensor for the CV learned via **PlaneAlign** is different than the dihedral angle.

Collective variable	Transition rate (ps ⁻¹)
Reference	$1.13 \pm 0.08 \times 10^{-2}$
Dihedral angle θ	1.41×10^{-2}
$(\sin \theta, \cos \theta)$	1.19×10^{-2}
$\cos \theta$	1.52×10^{-2}
ξ , BondAlign(2,3)	Metastable states not separated
ξ , PlaneAlign	1.25×10^{-2}

Table 2: Transition rates for the anti-gauche transition in both classical and machine-learned collective variables. We organize the ML CVs ξ according to the relevant feature map in use.

6 Discussion

In this work, we have made several contributions to the theory and application of quantitative coarse-graining. We established the equivalence between the orthogonality condition (OC), which naturally emerges as a mechanism for reducing the modeling error measured via

the relative entropy, and the Projected Orthogonality Condition (POC) (Proposition (2)), which ensures that the pathwise distance remains small. Through our study of butane, we also showed that Assumption 2 demanding that $D\xi D\xi^\top \succcurlyeq \delta_\xi^2 I_d$ can be relaxed to accommodate rank-deficient but non-degenerate collective variables (CVs), thereby broadening the applicability of these conditions.

We introduced a framework summarized in Algorithm 1 inspired by the orthogonality condition (OC), to construct CVs that flow along the surrogate manifold \mathcal{M} . A crucial component of our approach is the residence manifold learning algorithm (Algorithm 6), which carefully integrates several tools from manifold learning to construct a hypersurface representation. This structured approach facilitates an efficient computation of the normal vector, allowing for the direct construction of a CV whose gradients lie in the tangent space.

The significance of the feature map. The key emergent theme from this approach is the extreme importance of choosing the correct feature map for post-processing the data. The existence of several plausible but structurally different surrogate manifolds suggests that a more intricate design of feature maps beyond standard techniques such as RMSD alignment or pairwise distances can provide significant accelerations in downstream tasks such as transition rate estimation conducted in Section (5.4). In particular, our hand-crafted **PlaneAlign** feature map causes the diffusion net embedded to be parameterized by the dihedral angle θ . This parameterization is duly recovered by the collective variable ξ leading to a successful reproduction of the anti-gauche transition rate (see Table (2)). Furthermore, we provided a heuristic function **HyperSurface**, (65), which combines Laplacian coordinates to embed diffusion map manifolds as hypersurfaces irrespective of the choice of feature map (see Figures (8), and (9)). However, **HyperSurface** remains purely a heuristic because of (1) false negatives (for instance, **PlaneAlign** attains a low 2D score but is a good 2D embedding) and (2) self-intersections despite functional independence. We resolved the second issue by simultaneously promoting functional independence in Laplacian eigenfunctions through a neural network loss (70) leading to **LAPCAE**, enabling a well-structured embedding of the surrogate manifold (10).

Limitations. Despite the above advances, several limitations remain. Our current implementation has only been applied to the butane molecule, a very simple MD system. Moreover, in our framework, the orthogonality condition (OC) is imposed on the surrogate manifold rather than directly in the all-atom space \mathbb{R}^N . While it is theoretically possible to define an orthogonality condition in \mathbb{R}^N via a parameterization $\xi = \hat{\xi} \circ \Psi$ and a function $\Phi = \hat{\Phi} \circ \Psi$, we found this approach impractical. The presence of numerous ways to satisfy the constraint $\nabla \xi \cdot \nabla \Phi = 0$ in \mathbb{R}^N introduces excessive local minima in the loss function, making the learning of ξ less robust.

Can the surrogate manifold be a CV? Given the ability of diffusion maps to identify the slow manifold of the overdamped Langevin dynamics (1), the learned manifold coordinates Ψ could, in principle, serve as CVs. Similar ideas have been implemented in [Ryd24] or [Smi+18] where CVs are directly designed to optimize spectral criteria. Here we use eigenfunctions to reduce the problem to a surrogate space \mathbb{R}^{D+1} and then apply the relevant CV criteria in this surrogate space. We emphasize that enforcing the orthogonality condition (OC) remains beneficial despite the complexity reduction afforded by the map Ψ . In particular, the manifold coordinates Ψ may still be high-dimensional depending on the choice of embedding dimension $D + 1$, making direct usage impractical. Moreover, the orthogonality

condition (OC) provides an implicit way to encode functional dependence on the intrinsic parameterization of the surrogate manifold without requiring a coordinate chart in \mathbb{R}^{D+1} . Specifically, locally the surrogate manifold has $D + 1$ degrees of freedom and can be represented as the graph of a function. However, recovering such a function for every point is highly cumbersome and the orthogonality condition (OC) provides a way to implicitly define ξ on these intrinsic degrees of freedom.

Future applications and implementational improvements. The above insights and limitations open numerous directions of future work. One primary direction is to apply our methodology towards studying the conformational dynamics of synthetic peptide chains such as chignolin [HK11] or AIB9, and to the resolution of more advanced challenges such as cryptic pocket discovery or [WHT22] nucleation [Wan+24b]. Given the challenges of defining the orthogonality condition directly in \mathbb{R}^N , future work could explore alternative formulations that mitigate the issue of excessive local minima in the loss function. This may involve developing regularization techniques or optimizing over constrained subspaces that better capture physically meaningful CVs.

Open theoretical questions. In addition to applications in molecular dynamics, here we also underline some open questions in quantitative coarse-graining and manifold learning prompted by our approach. With regards to quantitative coarse-graining, in Section (3), we have demonstrated empirically that the diffusion tensor $M(z)$ need not be full rank to reproduce transition rates. This assumption is ubiquitous in most recent works on quantitative coarse-graining, thus leaving an intriguing avenue to extend the existing theory toward error estimates for degenerate diffusions. Moreover, with regards to manifold learning, we make use of group invariant diffusion maps via a group invariant feature map in Algorithm 6, thus furthering the project started in [RCS23; HK23] of encoding group structure into spectral embeddings. These works also use a group invariant kernel to perform diffusion maps but do so by imparting group invariance via averaging against the Haar measure of the underlying Lie group. This necessitates generating the orbit of every element in the input point cloud. Here we have presented an alternative approach that does not require these orbits by using a feature map before applying the kernel. A comparison and possible integration of both approaches is therefore interesting and may hold potential for accelerating the accuracy and expressibility of diffusion maps for MD data.

7 Conclusion

Our work advances the theory and practice of quantitative coarse-graining by elucidating the role of the orthogonality condition in reducing modeling error and preserving transition rates in overdamped Langevin dynamics. We introduced a learning framework that constructs collective variables by imposing the orthogonality condition on a surrogate space defined via manifold-based representations. We demonstrated that group invariant featurization is critical for defining such representations and therefore heavily affects coarse-graining performance. Through our butane case study, we demonstrated the role of analytical conditions from quantitative coarse-graining and provided practical heuristics, such as HyperSurface and LAPCAE, to address manifold learning challenges in our proposed algorithm. While our approach currently remains limited to simple systems and surrogate spaces, it opens

up rich avenues for applying these techniques to more complex biomolecular dynamics and exploring fundamental questions in coarse-graining and manifold learning.

8 Acknowledgements

This work was partially supported by AFOSR MURI grant FA9550-20-1-0397 and by NSF REU grant DMS-2149913. The first author would like to thank Akash Aranganathan and Dr. Eric Beyerle for helpful discussions regarding MD simulations in the high-friction regime.

Appendix

A Relation to full Langevin dynamics and reaction rate scaling

Typically, MD simulations track not just the positions X_t but also the velocities of atoms v_t (the lower case notation has been purposely chosen to not confuse with the potential V) under the *Langevin dynamics* given by

$$dX_t = v_t dt, \quad (\text{A-1})$$

$$m dv_t = -\gamma m v_t dt - \nabla V(X_t) dt + \sqrt{2k_B T \gamma} m^{1/2} dW_t. \quad (\text{A-2})$$

Here γ is the friction coefficient, T is the temperature, m is the diagonal matrix of masses of individual particles, and k_B is Boltzmann's constant used to make terms dimensionless. In the regime $\gamma \gg 1$, the Langevin dynamics (A-1), (A-2) may be approximated by the following anisotropic overdamped Langevin dynamics with $\beta^{-1} = k_B T$:

$$dX_t = -m^{-1} \nabla V(X_t) \gamma^{-1} dt + \sqrt{2\beta^{-1} \gamma^{-1}} m^{-1/2} dW_t. \quad (\text{A-3})$$

In this case, $\mu \propto \exp(-\beta V)$ is still the invariant measure. To remove the implicit effect of friction, we must rescale time as $\tau = \gamma^{-1}t$. This results in a time-rescaled overdamped Langevin dynamics given by

$$dX_\tau = -m^{-1} \nabla V(X_\tau) d\tau + \sqrt{2\beta^{-1}} m^{-1/2} dW_\tau. \quad (\text{A-4})$$

Under the overdamped approximation, the dynamics are anisotropic due to the involvement of the mass matrix m . In this case, the diffusion tensor must feature this mass rescaling [Cam13, Eq. 5] and thus be given by:

$$M(z) := \mathbb{E}_\mu[(D\xi)m^{-1}(D\xi)^\top \mid \xi = z]. \quad (\text{A-5})$$

With this diffusion tensor, the rate formula (48) applies for computing the transition rate ν'_{AB} . However, this transition rate is for transitions occurring in the timescale τ ; thus to recover the timescale t , we must rescale by the relevant factor of γ . This is pertinent when computing transition rates. For example, as a heuristic, the transition rate ν'_{AB} computed

for the dynamics (A-4) would be under the units $1/\tau = \gamma/t \iff t^{-1} = \gamma^{-1}\tau^{-1}$. Therefore, the transition rate ν_{AB} in the units t^{-1} (for instance, in ps^{-1}) may be recovered as

$$\nu_{AB} \approx \gamma^{-1} \nu'_{AB}. \quad (\text{A-6})$$

However, the reaction rate is not the only place where the friction coefficient must be accounted for, because the diffusion tensor M is calculated in practice also with a trajectory X_t indexed by time. This is due to the following reason: given z the string method [Mar+06] for computing the diffusion matrix $M(z)$ modifies the potential V with a harmonic restraint with stiffness κ :

$$V^z(x) := V(x) + \frac{\kappa}{2} \|z - \xi(x)\|_2^2. \quad (\text{A-7})$$

With the potential V^z , the process X_t^z is simulated according to the Langevin dynamics (A-1)-(A-2). Then the diffusion tensor is given by:

$$[M(z)]_{jk} := \lim_{T \rightarrow \infty} \frac{1}{T} \int_0^T \sum_{i=1}^{3N} m_i^{-1} \frac{\partial \xi_j(X_t^z)}{\partial x_i} \frac{\partial \xi_k(X_t^z)}{\partial x_i} dt \quad (\text{A-8})$$

$$= \lim_{T \rightarrow \infty} \frac{1}{T} \int_0^T \sum_{i=1}^{3N} m_i^{-1} \frac{\partial \xi_j(X_\tau^z)}{\partial x_i} \frac{\partial \xi_k(X_\tau^z)}{\partial x_i} \gamma d\tau \quad (\text{A-9})$$

$$\approx \frac{\gamma}{n} \sum_{\ell=1}^n \sum_{i=1}^{3N} m_i^{-1} \frac{\partial \xi_j(X_{\ell\Delta\tau}^z)}{\partial x_i} \frac{\partial \xi_k(X_{\ell\Delta\tau}^z)}{\partial x_i} \quad (\text{A-10})$$

$$= \frac{\gamma}{n} \sum_{\ell=1}^n \sum_{i=1}^{3N} m_i^{-1} \frac{\partial \xi_j(X_{\ell\gamma^{-1}\Delta t}^z)}{\partial x_i} \frac{\partial \xi_k(X_{\ell\gamma^{-1}\Delta t}^z)}{\partial x_i} \quad (\text{A-11})$$

The third line following the second is the essence of the string method. Here Δt is the time step used for simulating Langevin dynamics—the above calculation suggests that it needs to be additionally smaller to scale with the friction coefficient.

B Relevant differential geometry

Here we introduce some terms from Riemannian geometry used in Section 4.

Definition 3. *We define the Euclidean and standard Euclidean groups in three dimensions as follows:*

$$E(3) := \{g : \mathbb{R}^3 \rightarrow \mathbb{R}^3 \mid g(x) = Ox + b, O^\top O = I, b \in \mathbb{R}^3\}, \quad (\text{B-12})$$

$$SE(3) := \{g : \mathbb{R}^3 \rightarrow \mathbb{R}^3 \mid g(x) = Rx + b, R^\top R = I, \det(R) = 1, b \in \mathbb{R}^3\}. \quad (\text{B-13})$$

Thus, $E(3)$ comprises all translations, rotations, and reflections of \mathbb{R}^3 while $SE(3)$ comprises all rotations and translations.

Definition 4. Let $F : \mathcal{M} \rightarrow \mathcal{N}$ be a smooth map between smooth manifolds. The differential (or pushforward) of F at a point $p \in \mathcal{M}$ is the linear map

$$dF_p : T_p \mathcal{M} \rightarrow T_{F(p)} \mathcal{N} \quad (\text{B-14})$$

defined by its action on tangent vectors $X \in T_p \mathcal{M}$, satisfying

$$(dF_p X)(f) = X(f \circ F) \quad \text{for all } f \in C^\infty(\mathcal{N}). \quad (\text{B-15})$$

Definition 5. A smooth map $F : \mathcal{M} \rightarrow \mathcal{N}$ is an immersion at a point $p \in \mathcal{M}$ if its differential is injective:

$$\ker(dF_p) = \{0\} \Leftrightarrow dF_p \text{ is injective.} \quad (\text{B-16})$$

If this holds for all $p \in \mathcal{M}$, then F is called an immersion. Additionally, if F is a homeomorphism onto its image, then it is an embedding and \mathcal{M} is said to be embedded in \mathcal{N} .

Definition 6. Let \mathcal{N}^n be an n -dimensional smooth manifold. A hypersurface in \mathcal{N} is a smooth manifold \mathcal{M}^{n-1} of dimension $n-1$, together with an embedding

$$F : \mathcal{M}^{n-1} \hookrightarrow \mathcal{N}^n \quad (\text{B-17})$$

such that the image $F(\mathcal{M}) \subset \mathcal{N}$ has codimension 1, meaning:

$$\dim \mathcal{N} - \dim F(\mathcal{M}) = 1. \quad (\text{B-18})$$

Equivalently, a hypersurface can locally be described as the regular level set of a smooth function, i.e there exists an open set $V \subset \mathcal{N}$ and a smooth function $\varphi : V \rightarrow \mathbb{R}$ such that

$$\mathcal{M} \cap V = \{p \in \mathcal{N} : \varphi(p) = 0\}, \quad \text{with } d\varphi_p \neq 0 \text{ on } \mathcal{M} \cap V. \quad (\text{B-19})$$

Definition 7. Let $(\mathcal{N}^n, g), (\mathcal{M}^{n-1}, h)$ be a Riemannian manifolds, and let

$$F : \mathcal{M}^{n-1} \hookrightarrow \mathcal{N}^n \quad (\text{B-20})$$

be a smooth embedded hypersurface. A normal vector at a point $p \in \mathcal{M}$ is a nonzero vector $\nu_p \in T_{F(p)} \mathcal{N}$ such that

$$g_{F(p)}(\nu_p, dF_p(X)) = 0 \quad \text{for all } X \in T_p \mathcal{M}. \quad (\text{B-21})$$

Since \mathcal{M} is of codimension 1, the space of normal vectors is one-dimensional, and any two normal vectors differ by a scalar multiple.

C Computational details

The code for reproducing our results and accessing our trained models has been provided at https://github.com/ShashankSule/CV_learning_butane. Below we include details for the numerical computation of the committor function.

Results in Section 3. The transition rates in Table (1) were computed by numerically solving the boundary value problem (47) and then using a quadrature method for computing the integral (48). For ξ_1 , the dihedral angle, we discretized the elliptic operator \mathcal{L} with a Fourier difference stencil on 10^3 equispaced points in $[0, 2\pi]$. After computing the committor by imposing the relevant boundary conditions, we computed (48) using Simpson’s rule. For ξ_2 , i.e cosine of the dihedral angle, the committor problem amounts to solving the BVP (47) in the interval $(\cos(\pi - 0.2), \cos(\pi/3 + 0.1))$ with boundary conditions $q(\cos(\pi - 0.2)) = 0$, $q(\cos(\pi/3 + 0.1)) = 1$. To numerically solve this BVP, we used Chebyshev spectral differentiation, followed by Clenshaw-Curtis quadrature. Finally, for ξ_3 , we used a diffusion map-based solver for the committor function proposed for PDEs on manifolds in [ECT22; SEC23]. We then used Monte Carlo integration to compute the rate.

Neural network architectures and training. For each choice of the feature map, we train a diffusion net carrying the data to a surrogate space, then a confining potential vanishing on the surrogate manifold, and finally collective variable(s) which flow orthogonally to the gradients of the confining potential. Below, we enumerate the network architectures, optimizers, and hyperparameters used in training the models.

Feature map	Model	# neurons	Activation	Optimizer & lr	Training epochs	Hyper-parameters
	LAPCAE	[12, 32, 32, 32, 4]	Tanh	Adam, 1e-4	500	$\alpha_{LAPCAE}^{Enc} = 0.5$, $\alpha_{LAPCAE} = 2.0$
BondAlign (2,3)	$\hat{\Phi}$	[3, 30, 45, 32, 32, 1]	$x + \sin^2(x)$	Adam, 1e-3	1000	$\alpha_{Zero} = 1.0$ $\alpha_{normals} = 0.0$
	$\hat{\xi}_1$	$\hat{\xi}_1 = \partial_1 \hat{\Phi}$	$1 + \frac{2 \sin(x) \cos(x)}{2 \sin(x) \cos(x)}$	No training	N.A.	N.A.
PlaneAlign	$\hat{\xi}_2$	[3, 30, 45, 32, 32, 1]	$x^2 + \sin(x)$	Adam, 1e-2	500	$\alpha_{OC} = 1.0$
	DNet	[42, 32, 32, 32, 4]	Tanh	Adam, 1e-4	500	$\alpha_{DNet} = 1.0$
	$\hat{\Phi}$	[2, 30, 45, 32, 32, 1]	$x + \sin^2(x)$	Adam, 1e-3	1000	$\alpha_{Zero} = 1.0$ $\alpha_{normals} = 0.0$

Table 3: Architectures, optimizers, and hyperparameters for the neural networks trained in the paper.

The Free energy and the diffusion tensor with BondAlign(2,3) and PlaneAlign. In section (5) and table (2) we study transition rates for the anti-gauche transition from CVs learned via the feature maps BondAlign(2,3) and PlaneAlign. In Figures (15) and (16) we present the free energy landscapes and diffusion tensors for CVs obtained via algorithm (1)

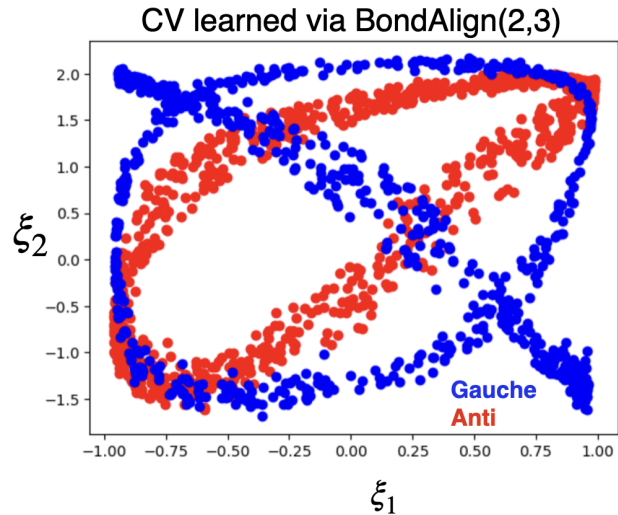


Figure 14: When visualizing data in the CV space learned with the BondAlign(2,3) feature map, the anti (red) and gauche (blue) states are not separated.

from data post-processed via these two feature maps.

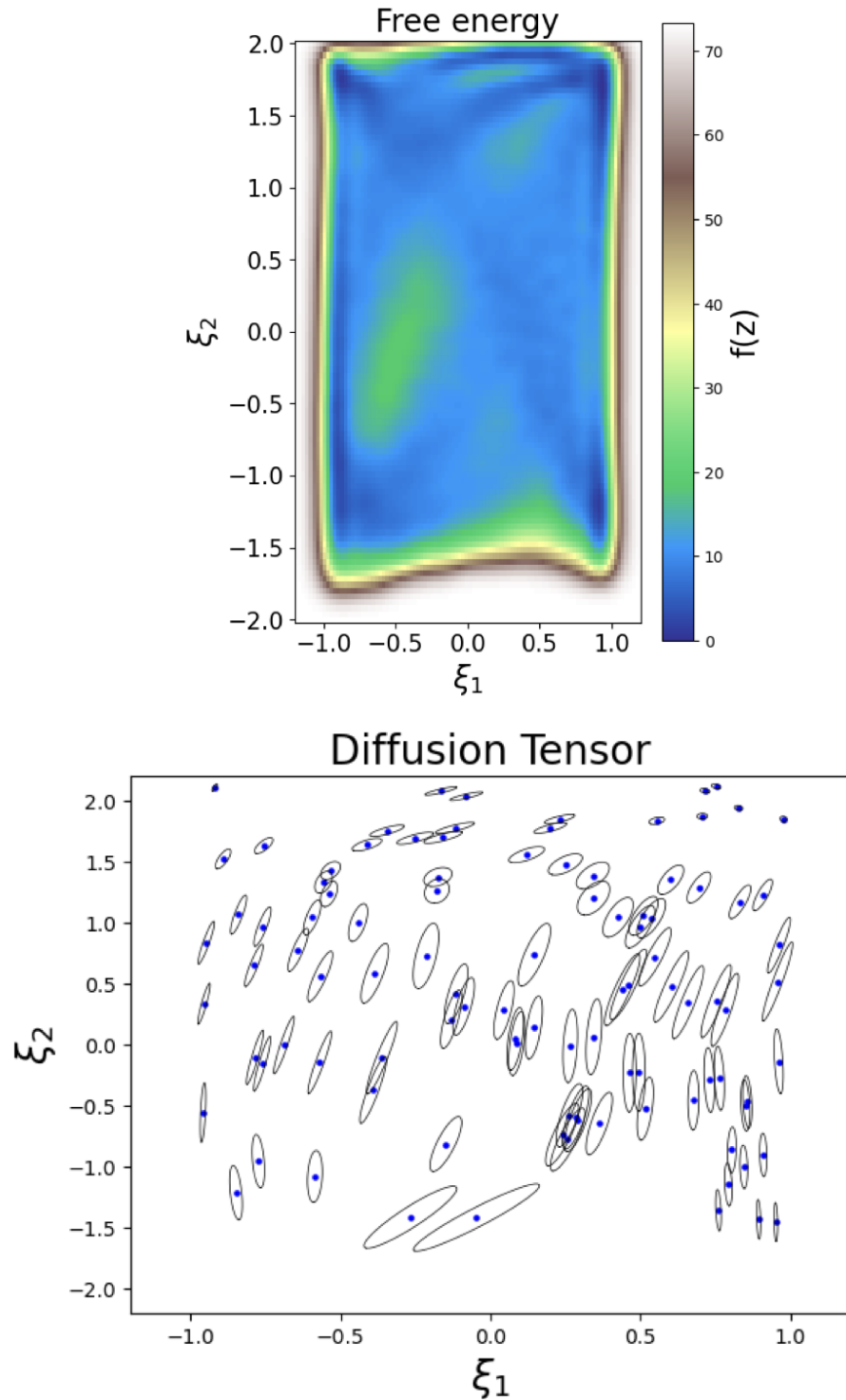


Figure 15: Free energy and diffusion tensor for BondAlign(2,3) with LAPCAE as the global coordinate chart parameterizing the resident manifold.

References

[ABG06] Hernan Alonso, Andrey A Bliznyuk, and Jill E Gready. “Combining docking and molecular dynamic simulations in drug design”. In: *Medicinal research reviews* 26.5 (2006), pp. 531–568.

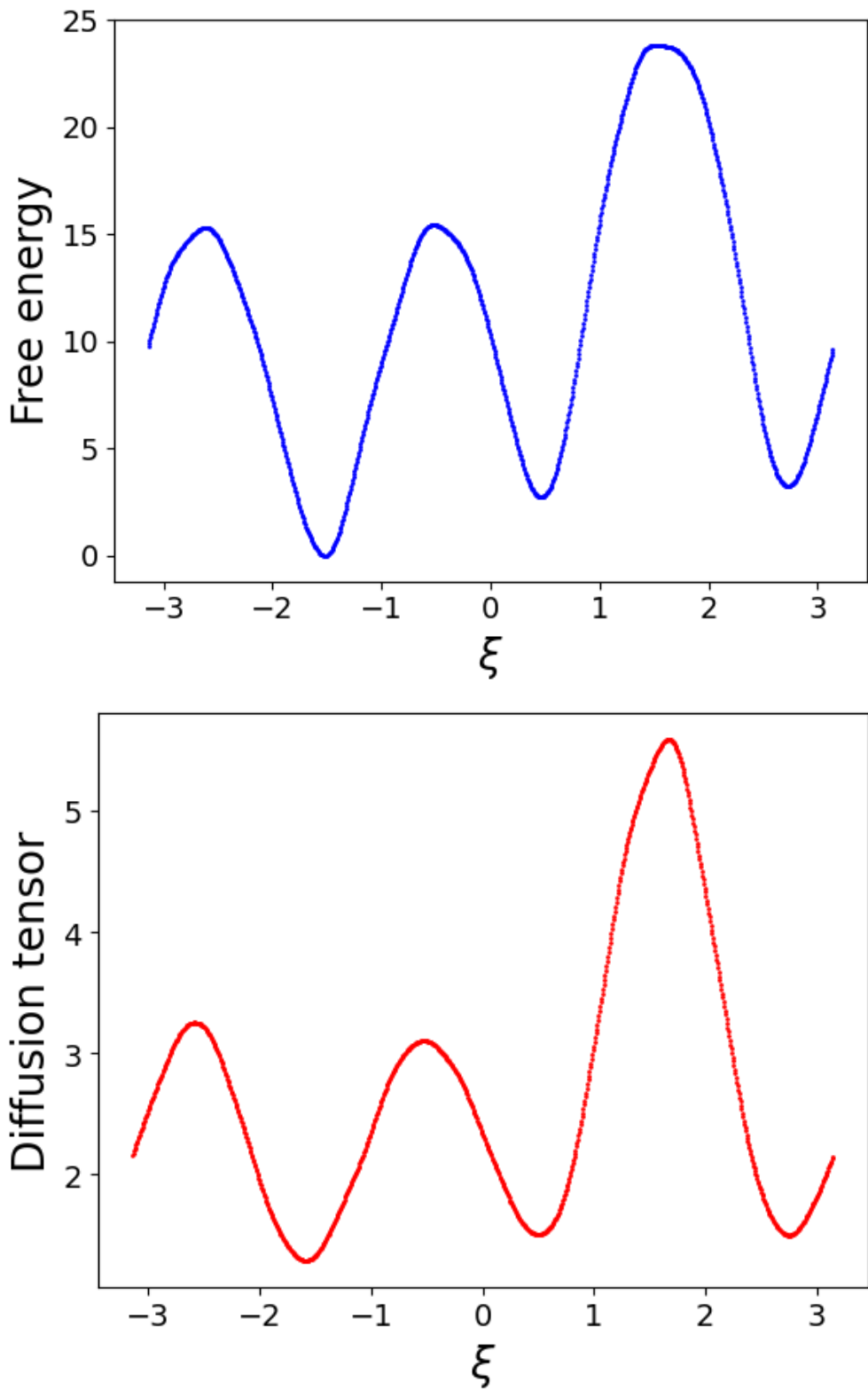


Figure 16: Free energy and diffusion tensor for PlaneAlign.

[Alt+08] Alex Altis, Martin Otten, Phuong H. Nguyen, Rainer Hegger, and Gerhard Stock. “Dihedral angle principal component analysis of molecular dynamics simulations”. In: *The Journal of Chemical Physics* 128.24 (2008), p. 245102.

[Bat14] Jonathan Bates. “The embedding dimension of Laplacian eigenfunction maps”. In: *Applied and Computational Harmonic Analysis* 37.3 (2014), pp. 516–530. ISSN: 1063-5203. DOI: <https://doi.org/10.1016/j.acha.2014.03.002>. URL: <https://www.sciencedirect.com/science/article/pii/S1063520314000426>.

[BBP08] Alessandro Barducci, Giovanni Bussi, and Michele Parrinello. “Well-tempered metadynamics: a smoothly converging and tunable free-energy method”. In: *Physical review letters* 100.2 (2008), p. 020603.

[Bel+23] Zineb Belkacemi, Marc Bianciotto, Hervé Minoux, Tony Lelièvre, Gabriel Stoltz, and Paraskevi Gkeka. “Autoencoders for dimensionality reduction in molecular dynamics: Collective variable dimension, biasing, and transition states”. In: *The Journal of Chemical Physics* 159.2 (2023).

[BPP21] Luigi Bonati, GiovanniMaria Piccini, and Michele Parrinello. “Deep learning the slow modes for rare events sampling”. In: *Proceedings of the National Academy of Sciences* 118.44 (2021), e2113533118.

[Cam13] Maria K Cameron. “Estimation of reactive fluxes in gradient stochastic systems using an analogy with electric circuits”. In: *Journal of Computational Physics* 247 (2013), pp. 137–152.

[CF18] Wei Chen and Andrew L Ferguson. “Molecular enhanced sampling with autoencoders: On-the-fly collective variable discovery and accelerated free energy landscape exploration”. In: *Journal of computational chemistry* 39.25 (2018), pp. 2079–2102.

[Cho+07] John D. Chodera, N. Singhal, Vijay S. Pande, Ken A. Dill, and William C. Swope. “Automatic discovery of metastable states for the construction of Markov models of macromolecular conformational dynamics”. In: *The Journal of Chemical Physics* 126.15 (2007), p. 155101.

[CL06] Ronald R Coifman and Stéphane Lafon. “Diffusion maps”. In: *Applied and computational harmonic analysis* 21.1 (2006), pp. 5–30.

[CM19] Yu-Chia Chen and Marina Meila. “Selecting the independent coordinates of manifolds with large aspect ratios”. In: *Advances in Neural Information Processing Systems* 32 (2019).

[Coi+08] Ronald R Coifman, Ioannis G Kevrekidis, Stéphane Lafon, Mauro Maggioni, and Boaz Nadler. “Diffusion maps, reduction coordinates, and low dimensional representation of stochastic systems”. In: *Multiscale Modeling & Simulation* 7.2 (2008), pp. 842–864.

[CPM15] Rémi Cuchillo, Kevin Pinto-Gil, and Julien Michel. “A collective variable for the rapid exploration of protein druggability”. In: *Journal of Chemical Theory and Computation* 11.3 (2015), pp. 1292–1307.

[CSF19] Wei Chen, Hythem Sidky, and Andrew L Ferguson. “Nonlinear discovery of slow molecular modes using state-free reversible VAMPnets”. In: *The Journal of chemical physics* 150.21 (2019).

[DRP08] Eric Darve, Daniel Rodríguez-Gómez, and Andrew Pohorille. “Adaptive biasing force method for scalar and vector free energy calculations”. In: *The Journal of Chemical Physics* 128.14 (2008), p. 144120. DOI: 10.1063/1.2829861.

[Duo+18] Manh Hong Duong, Agnes Lamacz, Mark A Peletier, André Schlichting, and Upanshu Sharma. “Quantification of coarse-graining error in Langevin and overdamped Langevin dynamics”. In: *Nonlinearity* 31.10 (2018), p. 4517.

[ECT22] Luke Evans, Maria K Cameron, and Pratyush Tiwary. “Computing committors via Mahalanobis diffusion maps with enhanced sampling data”. In: *The Journal of Chemical Physics* 157.21 (2022).

[EG92] L.C. Evans and R.F. Gariepy. *Measure Theory and Fine Properties of Functions. Studies in Advanced Mathematics*. Boca Raton: CRC Press, 1992.

[EV06] Weinan E and Eric Vanden-Eijnden. “Towards a theory of transition paths”. In: *Journal of statistical physics* 123.3 (2006), p. 503.

[FP17] Sean A. Fitzgerald and Michele Parrinello. “Diffusion tensors in collective variables spaces: Application to metadynamics”. In: *The Journal of Chemical Physics* 147.15 (2017), p. 152716. DOI: 10.1063/1.4998435.

[GKS04] Dror Givon, Raz Kupferman, and Andrew Stuart. “Extracting macroscopic dynamics: model problems and algorithms”. In: *Nonlinearity* 17.6 (2004), R55.

[GZ07] Alan Grossfield and Daniel M. Zuckerman. “Application of principal components analysis to distortion of biomolecular complexes”. In: *Theoretical Chemistry Accounts* 116 (2007), pp. 44–50.

[Hei+20] Nana Heilmann, Moritz Wolf, Mariana Kozlowska, Elaheh Sedghamiz, Julia Setzler, Martin Brieg, and Wolfgang Wenzel. “Sampling of the conformational landscape of small proteins with Monte Carlo methods”. In: *Scientific reports* 10.1 (2020), p. 18211.

[Her+18] Carlos X Hernández, Hannah K Wayment-Steele, Mohammad M Sultan, Brooke E Husic, and Vijay S Pande. “Variational encoding of complex dynamics”. In: *Physical Review E* 97.6 (2018), p. 062412.

[HK11] Ryuhei Harada and Akio Kitao. “Exploring the folding free energy landscape of a β -hairpin miniprotein, chignolin, using multiscale free energy landscape calculation method”. In: *The Journal of Physical Chemistry B* 115.27 (2011), pp. 8806–8812.

[HK20] Konrad Hinsen and Gerald R. Kneller. “Hydrogen bonds vs RMSD: Geometric reaction coordinates for the simulation of conformational transitions”. In: *The Journal of Chemical Physics* 162.7 (2020), p. 074107.

[HK23] Paulina Hoyos and Joe Kileel. “Diffusion maps for group-invariant manifolds”. In: *arXiv preprint arXiv:2303.16169* (2023).

[HNS20] Carsten Hartmann, Lara Neureither, and Upanshu Sharma. “Coarse graining of nonreversible stochastic differential equations: Quantitative results and connections to averaging”. In: *SIAM Journal on Mathematical Analysis* 52.3 (2020), pp. 2689–2733.

[Kar+21] Tarak Karmakar, Michele Invernizzi, Valerio Rizzi, and Michele Parrinello. “Collective variables for the study of crystallisation”. In: *Molecular Physics* 119.19-20 (2021), e1893848.

[Kev+24] George A Kevrekidis, Mauro Maggioni, Soledad Villar, and Yannis G Kevrekidis. “Thinner Latent Spaces: Detecting dimension and imposing invariance through autoencoder gradient constraints”. In: *arXiv preprint arXiv:2408.16138* (2024).

[LL10] Frédéric Legoll and Tony Lelièvre. “Effective dynamics using conditional expectations”. In: *Nonlinearity* 23.9 (2010), p. 2131.

[LLO17] Frédéric Legoll, Tony Lelièvre, and Stefano Olla. “Pathwise estimates for an effective dynamics”. In: *Stochastic Processes and their Applications* 127.9 (2017), pp. 2841–2863.

[LLS19] Frédéric Legoll, Tony Lelièvre, and Upanshu Sharma. “Effective dynamics for non-reversible stochastic differential equations: a quantitative study”. In: *Nonlinearity* 32.12 (2019), p. 4779.

[LZ19a] T. Lelièvre and W. Zhang. “Pathwise estimates for effective dynamics: The case of nonlinear vectorial reaction coordinates”. In: *Multiscale Modeling & Simulation* 17.3 (2019), pp. 1019–1051. DOI: [10.1137/18M1216793](https://doi.org/10.1137/18M1216793).

[LZ19b] Tony Lelièvre and Wei Zhang. “Pathwise estimates for effective dynamics: the case of nonlinear vectorial reaction coordinates”. In: *Multiscale Modeling & Simulation* 17.3 (2019), pp. 1019–1051.

[Mar+06] Luca Maragliano, Alexander Fischer, Eric Vanden-Eijnden, and Giovanni Cicotti. “String method in collective variables: Minimum free energy paths and isocommittor surfaces”. In: *The Journal of chemical physics* 125.2 (2006).

[Mar+18] Andreas Mardt, Luca Pasquali, Hao Wu, and Frank Noé. “VAMPnets for deep learning of molecular kinetics”. In: *Nature communications* 9.1 (2018), p. 5.

[Mis+19] Gal Mishne, Uri Shaham, Alexander Cloninger, and Israel Cohen. “Diffusion nets”. In: *Applied and Computational Harmonic Analysis* 47.2 (2019), pp. 259–285.

[MP17] Mohammad M. Sultan and Vijay S Pande. “tICA-metadynamics: accelerating metadynamics by using kinetically selected collective variables”. In: *Journal of chemical theory and computation* 13.6 (2017), pp. 2440–2447.

[Mül+21] Kai R. Müller, Wenkai Zhang, Madhusudhanan Krishnamoorthy, Cecilia Clementi, and Frank Noé. “Estimating the diffusion tensor of collective variables from short molecular dynamics trajectories”. In: *The Journal of Chemical Physics* 154.23 (2021), p. 234111. DOI: [10.1063/5.0051910](https://doi.org/10.1063/5.0051910).

[Neh+22] Neha, Vikas Tiwari, Soumya Mondal, Nisha Kumari, and Tarak Karmakar. “Collective Variables for Crystallization Simulations—from Early Developments to Recent Advances”. In: *ACS omega* 8.1 (2022), pp. 127–146.

[NN13] Frank Noé and Feliks Nüske. “A variational approach to modeling slow processes in stochastic dynamical systems”. In: *Multiscale Modeling & Simulation* 11.2 (2013), pp. 635–655.

[Nus+14] Feliks Nüske, Bettina G Keller, Guillermo Pérez-Hernández, Antonia SJS Mey, and Frank Noé. “Variational approach to molecular kinetics”. In: *Journal of chemical theory and computation* 10.4 (2014), pp. 1739–1752.

[OA23] Koji Ooka and Munehito Arai. “Accurate prediction of protein folding mechanisms by simple structure-based statistical mechanical models”. In: *Nature Communications* 14.1 (2023), p. 6338.

[PC14] Jordane Preto and Cecilia Clementi. “Fast recovery of free energy landscapes via diffusion-map-directed molecular dynamics”. In: *Physical Chemistry Chemical Physics* 16.36 (2014), pp. 19181–19191.

[Pér+13] Guillermo Pérez-Hernández, Fabian Paul, Toni Giorgino, Gianni De Fabritiis, and Frank Noé. “Identification of slow molecular order parameters for Markov model construction”. In: *The Journal of Chemical Physics* 139.1 (2013), p. 015102.

[PM13] Dominique Perrault-Joncas and Marina Meila. “Non-linear dimensionality reduction: Riemannian metric estimation and the problem of geometric discovery”. In: *arXiv preprint arXiv:1305.7255* (2013).

[PNV19] Sanjib Paul, Nisanth N Nair, and Harish Vashisth. “Phase space and collective variable based simulation methods for studies of rare events”. In: *Molecular Simulation* 45.14-15 (2019), pp. 1273–1284.

[RA07] P. R. Romero and G. E. Arnold. “Essential dynamics for the characterization of protein conformational ensembles”. In: *Current Opinion in Structural Biology* 17.2 (2007), pp. 169–174.

[RCS23] Eitan Rosen, Xiuyuan Cheng, and Yoel Shkolnisky. “G-invariant diffusion maps”. In: *arXiv preprint arXiv:2306.07350* (2023).

[Rib+18] João Marcelo Lamim Ribeiro, Pablo Bravo, Yihang Wang, and Pratyush Tiwary. “Reweighted autoencoded variational Bayes for enhanced sampling (RAVE)”. In: *The Journal of chemical physics* 149.7 (2018).

[Roh+11] Mary A. Rohrdanz, Wenwei Zheng, Mauro Maggioni, and Cecilia Clementi. “Determination of reaction coordinates via locally scaled diffusion map”. In: *The Journal of Chemical Physics* 134.12 (2011), p. 124116.

[Ryd24] Jakub Rydzewski. “Spectral map for slow collective variables, Markovian dynamics, and transition state ensembles”. In: *Journal of Chemical Theory and Computation* 20.18 (2024), pp. 7775–7784.

[SEC23] Shashank Sule, Luke Evans, and Maria Cameron. “Sharp error estimates for target measure diffusion maps with applications to the committor problem”. In: *arXiv preprint arXiv:2312.14418* (2023).

[SG21] Steffen Schultze and Helmut Grubmüller. “Time-lagged independent component analysis of random walks and protein dynamics”. In: *Journal of Chemical Theory and Computation* 17.9 (2021), pp. 5766–5776.

[Sha17] U. Sharma. “Coarse-graining of Fokker-Planck equations”. PhD thesis. Technische Universiteit Eindhoven, 2017. URL: https://pure.tue.nl/ws/files/51661644/20170112_Sharma.pdf.

[SK11] Vojtěch Spiwok and Blanka Králová. “Metadynamics in the conformational space nonlinearly dimensionally reduced by Isomap”. In: *The Journal of chemical physics* 135.22 (2011).

[SMH23] Subarna Sasmal, Martin McCullagh, and Glen M Hocky. “Reaction coordinates for conformational transitions using linear discriminant analysis on positions”. In: *Journal of chemical theory and computation* 19.14 (2023), pp. 4427–4435.

[Smi+18] Zachary Smith, Debabrata Pramanik, Sun-Ting Tsai, and Pratyush Tiwary. “Multi-dimensional spectral gap optimization of order parameters (SGOOP) through conditional probability factorization”. In: *The Journal of Chemical Physics* 149.23 (2018).

[SP13] Christian R. Schwantes and Vijay S. Pande. “Improvements in Markov state model construction reveal many non-native interactions in the folding of NTL9”. In: *Journal of Chemical Theory and Computation* 9.4 (2013), pp. 2000–2009.

[SP15] Christian R Schwantes and Vijay S Pande. “Modeling molecular kinetics with tICA and the kernel trick”. In: *Journal of chemical theory and computation* 11.2 (2015), pp. 600–608.

[VTP16] Omar Valsson, Pratyush Tiwary, and Michele Parrinello. “Enhancing important fluctuations: Rare events and metadynamics from a conceptual viewpoint”. In: *Annual review of physical chemistry* 67.1 (2016), pp. 159–184.

[VW19] Santosh Vempala and Andre Wibisono. “Rapid convergence of the unadjusted langevin algorithm: Isoperimetry suffices”. In: *Advances in neural information processing systems* 32 (2019).

[Wan+24a] Dedi Wang, Yunrui Qiu, Eric R Beyerle, Xuhui Huang, and Pratyush Tiwary. “Information bottleneck approach for Markov model construction”. In: *Journal of chemical theory and computation* 20.12 (2024), pp. 5352–5367.

[Wan+24b] Ruiyu Wang, Shams Mehdi, Ziyue Zou, and Pratyush Tiwary. “Is the local ion density sufficient to drive NaCl nucleation from the melt and aqueous solution?” In: *The Journal of Physical Chemistry B* 128.4 (2024), pp. 1012–1021.

[WHT22] Yihang Wang, Lukas Herron, and Pratyush Tiwary. “From data to noise to data for mixing physics across temperatures with generative artificial intelligence”. In: *Proceedings of the National Academy of Sciences* 119.32 (2022), e2203656119.

[WN18] Christoph Wehmeyer and Frank Noé. “Time-lagged autoencoders: Deep learning of slow collective variables for molecular kinetics”. In: *The Journal of chemical physics* 148.24 (2018).

[WT21] Dedi Wang and Pratyush Tiwary. “State predictive information bottleneck”. In: *The Journal of Chemical Physics* 154.13 (2021).

[WV04] E¹ Weinan and Eric Vanden-Eijnden. “Metastability, conformation dynamics, and transition pathways in complex systems”. In: *Multiscale modelling and simulation*. Springer, 2004, pp. 35–68.

[Yan+19] Yi Isaac Yang, Qiang Shao, Jun Zhang, Lijiang Yang, and Yi Qin Gao. “Enhanced sampling in molecular dynamics”. In: *The Journal of chemical physics* 151.7 (2019).

[Zha+19] Yue-Yu Zhang, Haiyang Niu, GiovanniMaria Piccini, Dan Mendels, and Michele Parrinello. “Improving collective variables: The case of crystallization”. In: *The Journal of chemical physics* 150.9 (2019).

[Zhe+13] Wenwei Zheng, Attilio Vittorio Vargiu, Mary A Rohrdanz, Paolo Carloni, and Cecilia Clementi. “Molecular recognition of DNA by ligands: Roughness and complexity of the free energy profile”. In: *The Journal of chemical physics* 139.14 (2013).

[ZHS16] Wei Zhang, Carsten Hartmann, and Christof Schütte. “Effective Dynamics along given Reaction Coordinates and Reaction Rate Theory”. In: *Faraday Discuss.* 195 (Oct. 2016). DOI: 10.1039/C6FD00147E.

[ZRC13] Wenwei Zheng, Mary A. Rohrdanz, and Cecilia Clementi. “Rapid exploration of configuration space with diffusion-map-directed molecular dynamics”. In: *The Journal of Physical Chemistry B* 117.42 (2013), pp. 12769–12776.

[ZS23] Wei Zhang and Christof Schütte. “Understanding recent deep-learning techniques for identifying collective variables of molecular dynamics”. In: *PAMM* 23.4 (2023), e202300189.

[ZS24] Wei Zhang and Christof Schütte. “On finding optimal collective variables for complex systems by minimizing the deviation between effective and full dynamics”. In: *arXiv preprint arXiv:2405.02001* (2024).